Biophysical Journal
Article

Biophysical Society

Membrane Tension Can Enhance Adaptation to Maintain Polarity of Migrating Cells

Cole Zmurchok,[1] Jared Collette,[2] Vijay Rajagopal,[2] and William R. Holmes[1,3,4,*]
[1]Department of Physics and Astronomy, Vanderbilt University, Nashville, Tennessee; [2]Department of Biomedical Engineering, University of Melbourne, Melbourne, Australia; [3]Department of Mathematics and [4]Quantitative Systems Biology Center, Vanderbilt University, Nashville, Tennessee

ABSTRACT Migratory cells are known to adapt to environments that contain wide-ranging levels of chemoattractant. Although biochemical models of adaptation have been previously proposed, here, we discuss a different mechanism based on mechanosensing, in which the interaction between biochemical signaling and cell tension facilitates adaptation. We describe and analyze a model of mechanochemical-based adaptation coupling a mechanics-based physical model of cell tension coupled with the wave-pinning reaction-diffusion model for Rac GTPase activity. The mathematical analysis of this model, simulations of a simplified one-dimensional cell geometry, and two-dimensional finite element simulations of deforming cells reveal that as a cell protrudes under the influence of high stimulation levels, tension-mediated inhibition of Rac signaling causes the cell to polarize even when initially overstimulated. Specifically, tension-mediated inhibition of Rac activation, which has been experimentally observed in recent years, facilitates this adaptation by countering the high levels of environmental stimulation. These results demonstrate how tension-related mechanosensing may provide an alternative (and potentially complementary) mechanism for cell adaptation.

SIGNIFICANCE Migratory cells, such as human neutrophils, encounter environments that contain wide-ranging levels of chemoattractant. To move, these cells must maintain an organized front-rear signaling polarity despite this wide variation in environmental stimuli. Past research has demonstrated a number of biochemical-based mechanisms by which cells adapt to variable signal levels. Here, we demonstrate that the interplay between Rho-family GTPase signaling and tension-mediated feedback loops may provide an alternative mechanochemical mechanism for adaptation to high levels of signaling.

INTRODUCTION

Human neutrophils and other migratory cells are able adapt to environments that contain wide-ranging levels of chemoattractant to maintain polarity. How does this adaptation occur? Models of adaptation based on biochemical processes such as receptor occupancy or receptor arrangement (1) have long been proposed. Here, we demonstrate that well-established mechanochemical interactions between Rac signaling and protrusion-related changes in cell tension can facilitate adaptation to maintain polarity when cells are exposed to wide-ranging levels of chemoattractant.

In the context of cell signaling, adaptation refers to the ability of cells to adjust to high levels of signaling or stimulation. Most signal response systems have a range of inputs over which they are sensitive to differences. When stimulus levels are sufficiently high to saturate the underlying regulatory system, the system loses its ability to distinguish signaling levels. For migration, cells must be able to adapt to higher stimulus levels as they proceed closer to the attractant source. In neutrophil migration, the Rho-family GTPase Rac rapidly polarizes to orient the cell in the direction of the stimulus (2,3). Interestingly, when these cells are subjected to high levels of stimulation, Rac first becomes highly activated throughout the cell and subsequently polarizes (3). Thus, in response to high levels of stimulation, these cells first adapt and then subsequently polarize. It has been previously demonstrated that feedback from cell tension to GTPase activation causes competition between multiple cellular protrusions (Fig. 1 *B*; (4,5)), ensuring that the cell

Submitted April 1, 2020, and accepted for publication August 25, 2020.
*Correspondence: william.holmes@vanderbilt.edu
Cole Zmurchok and Jared Collette contributed equally to this work.
Editor: Padmini Rangamani.
https://doi.org/10.1016/j.bpj.2020.08.035

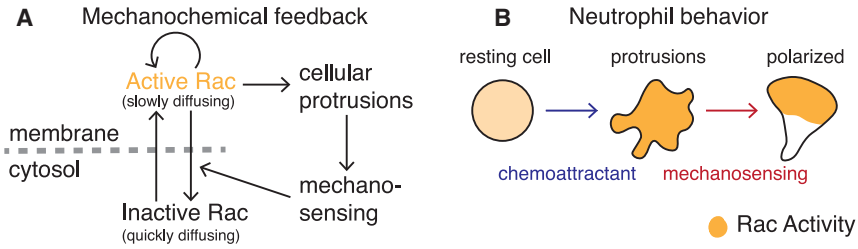

FIGURE 1 Overview of the mechanochemical feedback model and observed neutrophil behavior. (*A*) Schematic of mechanochemical feedback. Active (respectively inactive) Rac GTPases are assumed to be bound (respectively unbound) to the membrane and, therefore, slow (respectively fast) diffusing. Active Rac is autoactivated and causes cellular protrusions by activating downstream effectors. Cellular protrusions increase mechanosensing, which increases the deactivation rate of Rac. (*B*) Shown is a cartoon of the observed neutrophil behavior in a chemoattractive environment. A resting neutrophil is washed in chemoattractant, causing multiple sites of protrusive activity (within 20 s after stimulation). Subsequently, the cell adapts to the high signaling environment and polarizes to form a single leading front (~60 s after stimulation). (*B*) is adapted from Fig. 3 *B* of (5) and the timescales are estimated from Fig. 2 *A* of (3). To see this figure in color, go online.

protrudes in only one direction at a time. Here, we demonstrate that this feedback could also provide the cell with a form of mechanochemical adaptation to high, saturating levels of stimulation.

Our model mechanisms and results incorporate ideas related to adaptation, polarity, and tension regulation, each of which is well-studied in its own right. Adaptation has been primarily studied from a biochemical perspective. Models traditionally devised to explain the run-and-tumble behavior of bacterial chemotaxis (6) typically incorporate either negative feedback loops (7) or incoherent feed-forward loops (8) to achieve perfect adaptation to step changes in stimulus magnitude (9). These ideas were later combined with Meinhardt's concept of lateral inhibition for biological pattern formation (10) to explain how cells could adapt to environments and polarize in response to chemoattractant if the stimulus simultaneously triggered both a local excitatory activator and global inhibitor (11,12). This mechanism, known as LEGI (local excitation global inhibition), and variants have been extensively studied experimentally and theoretically (13–19). However, not all forms of adaptation are biochemical in nature. Cells can adapt to sustained mechanical stresses (20), for example, and large-scale cytoskeletal structures are known to lead to adaptive responses in cell migration to stiffness gradients in the environment (21).

Similarly, polarity regulation itself has seen sustained interest for multiple decades (22). Much (though not all) of this study has been dedicated to understanding the role of Rho GTPases, which regulate cytoskeletal remodeling, in polarity generation (23). The wave-pinning model of polarity (24–26), which we will build on here, demonstrated that the conservative activation and inactivation dynamics of these proteins are sufficient to explain the broad characteristics of the polarization process. The cell polarity and cell adaptation literature have been bridged by coupled models that exhibit both adaptive and polarity characteristics (19); however, such models are still biochemical in nature. More recently, models that couple single-cell mechanics and cytoskeletal mechanobiology with biochemistry have begun to explore the role of mechanochemical feedback loops on cell dynamics (3,4,27,28). However, the possible impact of cytoskeletal mechanics on adaptation during migration has yet to be explored.

Here, we build on the well-studied wave-pinning model of Rho GTPase dynamics (24–27,29–33) to analyze the consequences of feedback between signaling, cell protrusion (which affects tension), and tension. We include three critical assumptions into this model. First, Rac signaling (which is modeled using wave-pinning dynamics) promotes protrusion of the cell membrane through downstream activation of actin polymerization (23). Second, protrusion-related changes in cell surface area result in an increase or decrease in membrane tension. Third, membrane tension inhibits GTPase signaling (4,5,34–41). We combine these assumptions into a moving-boundary mechanochemical model (Fig. 1 *A*) that incorporates reaction-diffusion partial differential equations (PDEs) for Rac activity in a moving domain and a continuum-based description of cellular mechanics that affect the domain.

To understand the resulting model, we first use local perturbation analysis (LPA) (42,43) and numerical bifurcation analysis to analyze how tension changes resulting from changes in cell size influence GTPase signaling. Results indicate that increases in tension cause the cell to transit from an overstimulated to a polarizable regime of the GTPase signaling model. To test whether this adaptive response induces polarization, we use one-dimensional (1D) and two-dimensional (2D) minimal models to describe cellular physics and simulate the reaction-diffusion Rac signaling model in fully moving cells. Our purpose here is not to develop a high-fidelity model of cellular biophysics (see (44–55) for such models) or to propose an adaptation mechanism to replace biochemical models such as LEGI. Instead, our purpose is to use these models to assess how cell protrusions, tension, and GTPase signaling interact to provide an adaptive response that may act in parallel to other biochemical adaptation mechanisms. Both 1D and 2D simulations demonstrate that the feedback between signaling and tension does lead to adaptation in which the cell initially protrudes everywhere in response to a high stimulus but subsequently polarizes, as predicted. These results demonstrate that the feedback for establishment of polarity via membrane tension can be described using a wave-pinning model

of Rac signaling and, more importantly, that mechanosensing may (in addition to biochemical forms of adaptation) facilitate adaptation of migratory cells to high signaling levels.

MATERIALS AND METHODS

We will develop and analyze a model of the feedback between Rac signaling, cell size change, and tension changes. The purpose here is to use this model to study how these feedback loops may influence a cell's response to large stimuli. More specifically, we use this model to explore the hypothesis that these feedback loops provide a mechanochemical form of adaptation.

Here, we briefly outline the core elements of the model and analysis approach. We provide further details in subsequent sections. The model (illustrated in Fig. 1 *A*) builds on the well-studied wave-pinning model of Rho GTPase dynamics (24–27,29–33) to integrate tension effects resulting from changes in cell surface area. At a broad level, this model incorporates the cycling of Rac between activated (membrane-bound) and inactivated (cytosolic) states, Rac-mediated tension production (via cell protrusion), and tension-mediated inhibition of Rac activation (see below for further detail), all of which are well-established in neutrophil cells (4,5,34–41).

Because addressing the questions of interest here involves nonlinear interactions between signaling, shape change, and mechanics, we take several steps to analyze the dynamics of this system, with each building in additional complexity. First, we use the LPA (a form of spatio-temporal bifurcation analysis) to approximately map out the parametric dynamics of the system. Second, we study the effects of tension and cell size changes over time using 1D fixed domain simulations of the spatial PDE model in which tension and length are treated as parameters that we manually vary over time. This allows us to manually simulate tension to understand its potential effect on signaling dynamics. Third, we simulate a 1D moving-boundary version of the model in which Rac promotes protrusion, leading to cell size changes and tension effects. Finally, we simulate a 2D moving-boundary version of this model, coupling continuum mechanics with Rac signaling.

Reaction-diffusion Rac GTPase signaling model

We first describe the core model of Rac signaling that will be responsible for regulating protrusion in this model. We adopt the well-studied wave-pinning model (24–27,29–33) of GTPase activity. We consider Rac activity in a 1D or 2D domain with no-flux boundary conditions at the cell periphery and model the activity of both membrane-bound active Rac ($R(x,t)$) and freely-diffusing cytosolic inactive Rac ($R_i(x,t)$) forms as illustrated in the left part of Fig. 1 *A*. The nondimensionalized PDEs describing these dynamics in a stationary domain are as follows:

$$\frac{\partial R}{\partial t} = \left(b + c\frac{R^n}{1+R^n}\right)R_i - \delta R + D\Delta R, \tag{1a}$$

$$\frac{\partial R_i}{\partial t} = -\left(b + c\frac{R^n}{1+R^n}\right)R_i + \delta R + D_i\Delta R_i. \tag{1b}$$

The term in parentheses is a standard Hill function representation of autoactivation kinetics, with b representing a basal-activation rate and c the magnitude of autoactivation (i.e., positive feedback). The parameter δ is the deactivation rate, and D and D_i are the diffusion coefficients of the active and inactive forms, respectively. The ratio D/D_i is small because membrane-bound diffusion is slower than cytoplasmic diffusion. Because Rac cycles between inactive and active forms with no-flux boundary conditions, the total amount is conserved as a function of time: $\int R(x,t) + R_i(x,t)\,dx = R_T$. Full model and nondimensionalization details are in Supporting Materials and Methods.

External chemoattractant stimulation and feedback from tension

The two critical parameters of this model that we will focus on are the basal-activation rate b and the deactivation rate δ. The basal-activation rate will be used to encode the level of external stimulation applied to the cell. For example, application of a uniform stimulus will be modeled as an increase in the parameter b as the Rac signaling pathway becomes activated upon external stimulation. The δ parameter will be used to describe tension (T)-mediated inhibition of signaling:

$$\delta(T) = \delta_0 + \delta_1 T. \tag{2}$$

In cases in which we are not explicitly modeling tension, we will describe the effects of tension through changes in the parameter δ. For example, an increase in tension will be assumed to increase δ. Other functional forms (e.g., Hill functions) of $\delta(T)$ could, of course, be used. We use a linear function here for simplicity and to reduce the number of extraneous parameters in the model.

LPA, bifurcation analysis, and steady-state behavior

To approximately determine how stimulus level (b) and tension strength (δ) jointly affect the spatial dynamics of this system, we used LPA to analyze the behavior of the PDE model in the $b\delta$ plane. The LPA is an approximate asymptotic analysis that predicts whether the model (Eq. 1) will respond to a spatial perturbation (either small or large) and give rise to a spatial pattern formation. More specifically, it helps identify regions of parameter space associated with both linear instabilities (i.e., Turing regions) and stimulus-induced patterning (in which large stimuli are required for a response). The LPA has been demonstrated to be an effective analysis tool for studying GTPase and other systems (29,31,33,56–60). An explanation of the LPA method and a detailed step-by-step guide can be found in the "Computational Tools" article by Holmes et al. (43) and the references therein.

In practice, this method reduces the PDE system (Eq. 1) to an ordinary differential equation (ODE) system that approximately describes the dynamics of an asymptotically localized perturbation. By mathematically analyzing how the model system responds to this type of mathematically convenient perturbation, we can efficiently assess whether the model will give rise to spatial pattern formation and map its parameter space. This is carried out by studying the reduced LPA ODE system with numerical bifurcation software XPPAUT to determine the perturbed system's behavior in different parameter regimes (Fig. 2 *A*). Full details of the bifurcation analysis of the LPA ODE system can be found in Supporting Materials and Methods, including a corresponding one-parameter bifurcation diagram (Fig. S1).

1D mechanochemical model

Before moving to a full 2D changing domain model of the cell, we first develop a simpler 1D changing domain model to provide a preliminary analysis of the effects of tension and signaling feedback. To interrogate the mechanosensing-adaptation hypothesis in a moving, 1D cell, we couple the wave-pinning model for Rac activity to a simple spring-like mechanical model of the deforming cell. The underlying assumption here is that our simulated cells in 1D and 2D models capture the cell's substrate contact length or area that changes as the cytoskeleton is remodeled. We do not

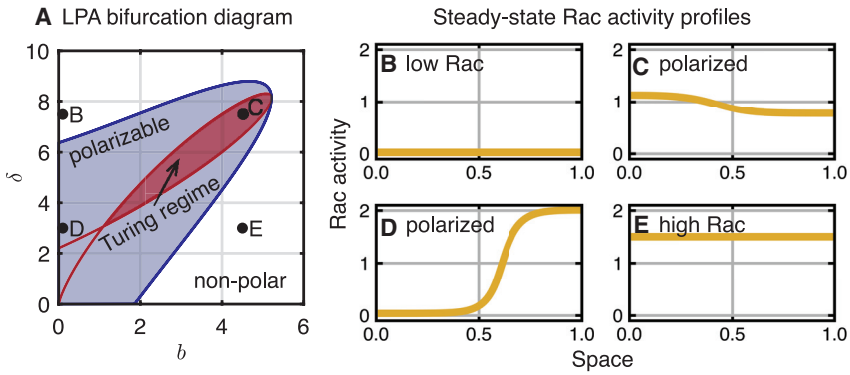

FIGURE 2 Parameter regimes of polar and nonpolar behavior and steady-state PDE solutions on a stationary domain. (*A*) The local perturbation analysis (LPA) reveals regimes of nonpolar (*unshaded*), stimulus-induced polarizable (*blue shaded*), and Turing unstable steady state, i.e., polarizable (*red shaded*), cell behavior in the $b\delta$ plane. The dots correspond to the parameters for steady-state Rac activity profiles in (*B*)–(*E*). (*B–E*) Shown are steady-state-simulated solutions to the PDEs. Initial conditions $R(x, 0) = 0$ except $R(x, 0) = 5$ for $x > 0.9$ are used in (*B*), (*D*), and (*E*). For (*C*), $R(x, 0) = 1 + \sin(4\pi x)/10$ is used. Spatially homogeneous initial conditions were used for the inactive amount to ensure the total Rac (R_T) is preserved: $R_i(x, 0) = R_T - \int_0^1 R(x,0)\,dx$. (*B*) Shown is the low Rac activity, $b = 0.1$ and $\delta = 7.5$. (*C*) Shown is the polarized Rac activity, $b = 0.1$ and $\delta = 3$. (*D*) Shown is the polarized Rac activity in the Turing regime, $b = 4.5$ and $\delta = 7.5$. (*E*) Shown is the high Rac activity, $b = 4.5$ and $\delta = 3$. The other parameters are $D = 0.01$, $D_i = 10$, $c = 5$, $n = 6$, and $R_T = 2$. To see this figure in color, go online.

explicitly model cell volume because the three-dimensional aspect is negligible in crawling cells on a 2D substrate, and the predominant dynamics occur on the 2D substrate contact area.

This minimal 1D deforming cell model consists of two components: 1) an overdamped, elastic spring model of the cell and 2) an adapted version of the Rac model to appropriately account for the changing domain. These are coupled with two conditions. First, we assume that active Rac at the cell ends can exert a protrusive force on the cell that opposes the restoring linear elastic spring force. This protrusive force depends sigmoidally on Rac activity at the end points. Second, the deactivation rate δ increases linearly with tension according to Eq. 2. Here, we define tension to be the difference between the cell length $L(t)$ and rest length ℓ_0: $T = L(t) - \ell_0$. Together, these assumptions result in a moving-boundary problem in which the Rac activity is transported within a time-dependent domain $\Omega(t) = [x_-(t), x_+(t)]$:

$$\frac{\partial R}{\partial t} + \frac{\partial}{\partial x}(aR) = \left(b + c\frac{R^n}{1+R^n}\right)R_i - \delta(T)R + D\frac{\partial^2 R}{\partial x^2}, \tag{3a}$$

$$\frac{\partial R_i}{\partial t} + \frac{\partial}{\partial x}(aR_i) = -\left(b + c\frac{R^n}{1+R^n}\right)R_i + \delta(T)R + D_i\frac{\partial^2 R_i}{\partial x^2}, \tag{3b}$$

with no-flux boundary conditions. We can determine the velocity field $a(x,t)$ throughout the cell body from the forces imposed at the cell ends because we assume that the cell changes length isotropically (as in (61–64)). This assumption means that as the cell length, $L(t) = x_+(t) - x_-(t)$, changes, each Lagrangian volume element will change proportionally to the total length change (this is a simplifying approximation that will be relaxed in the 2D model to follow). This relation specifies the flow a so that Rac is transported in the domain accordingly. Full model details can be found in Supporting Materials and Methods.

We assume that the movement of the cell's end points depends on a linear elastic restoring force and protrusive forces determined by Rac activity at the end points:

$$\gamma\frac{dx_-}{dt} = k(x_+ - x_- - \ell_0) - F_-(R(x_-(t), t)), \tag{4a}$$

$$\gamma\frac{dx_+}{dt} = -k(x_+ - x_- - \ell_0) + F_+(R(x_+(t), t)). \tag{4b}$$

Here, γ is the viscosity, k is the spring constant, ℓ_0 is the rest length of the spring, and the functions $F_\pm$ describe the protrusive forces oriented outward from the cell from R. Note that inertial effects are ignored as appropriate for modeling cell motion. We use a smoothed Heaviside function for the Rac-dependent force function $F_\pm(R)$:

$$F_\pm(R) = \frac{f_R}{1 + e^{-2s_1(R-s_0)}}. \tag{5}$$

The parameters s_1 and s_0 control the sharpness and location of the switch, respectively, and $f_R > 0$ is the magnitude of the force due to Rac activity.

2D mechanochemical model

We use a 2D continuum mechanics model coupled to reaction-diffusion PDEs for Rac activity to simulate 2D moving cells. The domain can freely deform in response to Rac activity and mechanics (these changes are no longer uniform as in 1D) because we assume that Rac activity leads to expansion in the normal direction. For Rac activity within the domain, we assume that the diffusion of active and inactive Rac is isotropic and leave the reactions (Eq. 1) unchanged.

To describe the mechanical model of the cell, we use the conservation of linear momentum from continuum mechanics. The inertial terms are neglected, leading to an approximation of first-order dynamics. This dynamical model relates the Cauchy stress $\boldsymbol{\sigma}$ and displacement $\boldsymbol{u}$ fields:

$$\nabla\cdot\boldsymbol{\sigma} + \gamma\dot{\mathbf{u}} = 0, \tag{6}$$

where γ is the Stokes damping coefficient that represents the viscous forces in the extracellular environment that resist cell motion and $\dot{\boldsymbol{u}}$ denotes the time derivative of displacement. We assume that intracellular strains are captured by the standard linear Kelvin-Voigt viscoelastic constitutive relation and, therefore, decompose $\boldsymbol{\sigma} = \boldsymbol{\sigma}^e + \boldsymbol{\sigma}^v$ into the elastic stress $\boldsymbol{\sigma}^e$ and viscous stress $\boldsymbol{\sigma}^v$. The elastic and viscous stresses are related to the strain $\boldsymbol{\varepsilon}$ through linear isotropic constitutive models, respectively:

$$\boldsymbol{\sigma}^e = \lambda\mathrm{tr}(\boldsymbol{\varepsilon})\mathbf{I} + 2\mu\boldsymbol{\varepsilon} \quad \text{and} \quad \boldsymbol{\sigma}^v = \beta(\lambda\mathrm{tr}(\dot{\boldsymbol{\varepsilon}})\mathbf{I} + 2\mu\dot{\boldsymbol{\varepsilon}}). \tag{7}$$

Here, $\mathbf{I}$ is the identity tensor, λ and μ are the Lamé coefficients that are related to the Young's modulus E and Poisson's ratio ν, and β is a viscous parameter related to the first and second coefficients of viscosity β_λ and β_μ (see Supporting Materials and Methods for full details). We also use the 2D plane stress conditions by assuming the z-directional thickness of the cell is

small relative to the expanding area and contains no z-directional stresses. Last, we use the infinitesimal, small-strain approximation for the kinematic relationship between the strain and displacement:

$$\boldsymbol{\varepsilon} = \frac{1}{2}\left(\nabla \boldsymbol{u} + (\nabla \boldsymbol{u})^T\right). \tag{8}$$

The mechanical model is coupled to Rac activity through the same conditions as in the 1D context but with three modifications. First, we assume the protrusive force from active Rac acts normal to the membrane boundary at any given point. Second, the deactivation rate now depends on a proxy for 2D tension, $T = A(t) - A_0$, the difference between the area $A(t)$ and rest area A_0. Third, we account for the deforming mechanical domain in the solution of the reaction-diffusion system as follows. The kinematic relationship between an initial and deformed geometry in the mechanical model is described by the deformation gradient tensor $\boldsymbol{F} = \mathbf{I} + (\partial \boldsymbol{u}/\partial \bar{\boldsymbol{x}})$ and its determinant $J = \det(\boldsymbol{F})$. This relationship can be used to map the spatial and temporal differential operators, and allows the reaction-diffusion equations to be solved on a stationary reference domain with fixed coordinates $\bar{\mathbf{x}}$:

$$\left.\frac{\partial R}{\partial t}\right|_{\bar{\mathbf{x}}} = DJ^{-1}\nabla_{\bar{\mathbf{x}}} \cdot \left(J\boldsymbol{F}^{-1}\boldsymbol{F}^{-T}\nabla_{\bar{\mathbf{x}}}R\right) + f(R, R_i) - RJ^{-1}\frac{\partial J}{\partial t}, \tag{9a}$$

$$\left.\frac{\partial R_i}{\partial t}\right|_{\bar{\mathbf{x}}} = D_iJ^{-1}\nabla_{\bar{\mathbf{x}}} \cdot \left(J\boldsymbol{F}^{-1}\boldsymbol{F}^{-T}\nabla_{\bar{\mathbf{x}}}R_i\right) - f(R, R_i) - R_iJ^{-1}\frac{\partial J}{\partial t}, \tag{9b}$$

where the function f describes the wave-pinning reaction kinetics as before: $f(R,R_i) = (b + c(R^n/1 + R^n))R_i$. Full model details can be found in the Supporting Materials and Methods.

Numerical methods

For the 1D model, we used a method of lines discretization with centered differences in space and the Python function odeint from SciPy (65) to integrate the resulting ODE system in time (odeint solves a system of ODEs using LSODA from the FORTRAN library odepack that automatically switches between stiff and nonstiff methods (66,67)) and Matplotlib (68) for visualization. We generated the steady-state Rac activity profiles in Fig. 2, *B–E* with this method using $N = 1000$ spatial grid points and integrated until time $t = 100$. We used the same method for all 1D PDE numerics; however, we adapted the scheme for time-dependent parameters and to simulate the mechanochemical model. To do so, we first transformed the moving-boundary problem to a stationary domain. Next, we solved the stationary-domain problem while simultaneously solving additional ODEs for the location of the cell's end points. By reversing the transformation, we can obtain the full moving-boundary solution. This method is similar to that used in other investigations of pattern formation on time-dependent domains (61–64).

We used the finite element method to solve the 2D mechanochemical model on the stationary reference domain (a circle of area 1) using the Python interface of the open source finite element modeling package FEniCS (69). We used standard linear Lagrange elements for the reaction-diffusion PDE and standard quadratic Lagrange elements for the mechanics equations with a mesh containing 4438 elements and 2325 nodes. In each time-step, we first solved the mechanics equations to obtain the displacement. Second, we calculate the deformation gradient tensor $\boldsymbol{F}$ and Jacobian $J = \det(\boldsymbol{F})$. Last, using these values, we solved the reaction-diffusion PDE (Eq. 9) using a first-order backward Euler time-stepping scheme with $\Delta t = 0.1$ and FEniCS solve command with default parameters (FEniCS automatically solves the linear mechanics problem and uses Newton's method for the nonlinear reaction-diffusion problem). Finally, we transform the solution to the moving cell by displacing the stationary domain according to the displacements obtained from solving the mechanics equation.

We validated the numerical methods in both 1D and 2D by checking for Rac mass conservation over time for each simulation and by checking that the mass conservation error decreases as the spatial resolution increases (Figs. S2 and S3). Polarity is assessed in two ways. First, we calculate the difference between maximal and minimal Rac activity throughout the domain. If this difference is sufficiently high (>0.1) we consider the cell polarized. Second, we plot and calculate the interquartile range (IQR) of the distribution of Rac activity throughout the cell at a given time. Polarized cells have relatively large IQR and bimodal Rac activity distributions, whereas nonpolar cells have smaller IQR and unimodal Rac activity. See Supporting Materials and Methods for full details.

Parameters

We nondimensionalized the Rac signaling PDEs (see Supporting Materials and Methods for details) because quantitative estimates of these parameters are not available. The Rac signaling parameters ($R_T = 2$, $n = 6$, and $c = 5$, respectively) were chosen to be consistent with prior studies (31) of the wave-pinning motif that ensure a large polarizable region in the $b\delta$ plane (basal-activation rate b and deactivation rate δ). We set $D = 0.01$ and $D_i = 10$ for our simulations because we are working with a unit length cell, and it is known that the active and inactive forms have diffusion length scales much smaller and larger, respectively, than the cell size (26). These reaction-diffusion parameters are used in both 1D and 2D simulations.

For the 1D mechanical model, we chose damping coefficient γ and spring constant k so that viscous drag dominates the elastic restoring force with $\gamma = 1$ and $k = 0.01$ consistent with estimates that friction dominates elastic forces by several orders of magnitude (64). Finally, we chose the force magnitude from Rac, $f_R = 0.001$, and switch parameters, $s_0 = 1$ and $s_1 = 10$, so that changes in the cell length are smaller and slower compared with Rac activity and such that the cell length changes are less than 10% of the original length when Rac is uniformly highly activated throughout the domain. This relatively small but significant area change is similar to that observed in experiments (3).

For the 2D mechanical model, we used $E = 0.3$ kPa for the Young's modulus as estimated for HL-60 cells (70) that serve as a valid model system for human neutrophils (71) and $\nu = 0.45$ for the Poisson's ratio ($\nu = 0.499$ represents incompressibility). The viscous parameter $\beta = 10$ s is the ratio of the viscosity of the internal actin cytoskeleton $\beta_\mu = 1$ kPa•s (72) and shear modulus $\mu \approx 0.1$ kPa (calculated from E and ν). To determine the magnitude of the force due to Rac activity f_R, we started with the maximal force due to actin polymerization of 0.8 nN/μm (73), and subsequently, we chose $f_R = 0.3$ nN/μm along with switch parameters $s_0 = 1$ and $s_1 = 10$ so that the cell area changes are around or less than 30% of the original area when Rac is uniform and highly activated throughout the domain as in Fig. 6 *A*. This ensures that dilution effects (as the cell expands, conserved Rac becomes more dilute) to Rac signaling dynamics are minimized. Finally, we estimated the Stokes damping coefficient $\gamma = 20$ kPa•s/μm^2 so that our simulated cells in Fig. 6 *B* move with velocity ≈ 0.17 μm/s (1 spatial unit in 60 s $\approx$ 10 μm in 60 s) that is within the velocity range of migrating neutrophils in experiments 0.1–0.2 μm/s (71,74).

RESULTS

LPA and steady-state behavior of the Rac signaling model

We first use the LPA to approximately map the dynamics of the signaling system in the $b\delta$ plane. Results show that the $b\delta$ plane can be divided into three regions (Fig. 2 *A*): 1) a

nonpolar regime in which the only stable solutions to the PDE are homogeneous steady states that correspond to a uniform Rac activity level across the cell; 2) a polarizable regime in which a sufficiently large spatially heterogeneous stimulus can result in the formation of a polarized pattern; and 3) a Turing regime in which the homogeneous steady states are linearly unstable, leading to polarization. Numerical simulations of the full PDE system verify the presence of these different regimes. Fig. 2, *B–E* illustrates the stable steady-state Rac distributions at the four marked points in Fig. 2 *A*. In the case of point C, random noise from the homogeneous steady state is sufficient to generate patterning (here, we used a small amplitude sine function). For D, a large heterogeneous perturbation is required, consistent with the LPA prediction. Neither B nor E is capable of polarizing.

Proof of concept: fixed domain, 1D model with manually varied tension

The bifurcation structure in Fig. 2 *A* suggests a possible mechanism for adaptation in the presence of high levels of signaling. Consider a high level of chemoattractant that over-stimulates a cell, leading to uniform Rac activation and protrusions across the periphery. In modeling terms, this would correspond to an increase in the basal-activation parameter (b), as illustrated in Fig. 3 *A*. This broad protrusion would lead to an increase in tension (and the parameter δ), moving the model cell back into the polarization regime. In this way, uniform high levels of stimulation would initially lead to cell wide protrusion that later gives way to polarization as observed experimentally. In the coming sections, we explore this idea in more detail.

To begin, we first simulate the 1D spatial version of this model on a fixed domain. Because the domain is fixed, we do not model cell size change and tension changes explicitly but rather temporally change parameters to account for those effects. To mimic uniform stimulation followed by tension build up, we temporally vary the model parameters in two phases. First, b is increased to mimic stimulation, as indicated by the horizontal arrow on Fig. 3 *A*. Second, we gradually increase δ after the vertical arrow. Fig. 3 *B* shows the results of this simulation. The initial resting cell becomes highly uniformly stimulated upon onset of stimulation. As tension builds up, uniform Rac activation levels decrease. Finally, without the application of any further perturbation, the model cell polarizes. This suggests that the mechanism of expansion followed by tension build up may facilitate adaptation to high signaling levels. This modeling experiment acts as a proof of concept of the mechanosensing-adaptation hypothesis.

1D mechanochemical moving-boundary model demonstrates tension-mediated adaptation

Using the 1D mechanochemical model, we mimicked the simulation depicted by the arrows in Fig. 3 *A*. A cell at rest (uniform Rac activity and stable length) is stimulated by suddenly increasing b. From this point on, all cellular changes are driven by the mechanochemical model. Fig. 4, *B–D* demonstrates the results of three simulations that yield distinct results after an initial period of uniform expansion. In Fig. 4 *B*, there is no tension-mediated deactivation ($\delta_1 = 0$), and the cell expands approximately by 10% but does not polarize. In Fig. 4 *C*, there is feedback from tension ($\delta_1 = 80$), and as predicted by prior simulations, after the cell has sufficiently expanded, tension increases lead to polarization. This confirms the plausibility of this mechanosensing-adaptation hypothesis in a 1D deforming cell model.

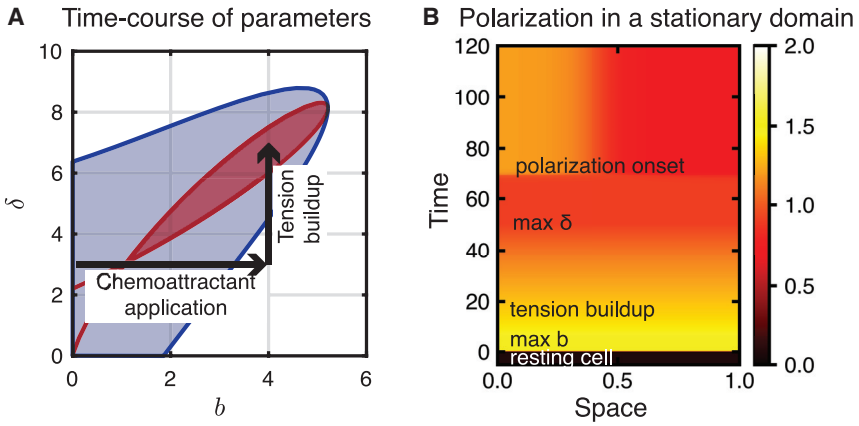

FIGURE 3 Time-dependent parameters on a stationary domain mimic observed neutrophil behavior. (*A*) Shown is the trajectory of time-dependent parameters in the $b\delta$ plane mimicking uniform activation followed by increased tension-mediated inactivation. The shaded blue and red regions are the same as in Fig. 2 *A*. Note that for a wide-range of parameter values, a change in δ (moving vertically across the bifurcation diagram) can push the cell into the polarizable or Turing regime in response to a change in chemoattractant levels, which modulate the activation of Rac through the parameter b (moving horizontally). (*B*) Shown is the kymograph of Rac activity in a stationary-domain simulation for these time-dependent parameters. The cell is at rest for $t < 0$ with $b = 0.1$ and $\delta = 3$ (other parameters as in Fig. 2). For $0 < t < 5$ ("max b"), the cell is stimulated with uniform chemoattractant $b = 4$ and jumps to the high Rac homogeneous steady state. For $5 < t < 50$ ("tension buildup"), δ increases linearly in time: $\delta(t) = 3 + 4/45(t - 5)$ to reach a maximum of 7 at $t = 50$ ("max δ"). As a result of the increasing δ, the system re-polarizesdue to numerical error because the homogeneous steady state is linearly unstable with parameters in the Turing regime ("polarization onset"). See Video S1. To see this figure in color, go online.

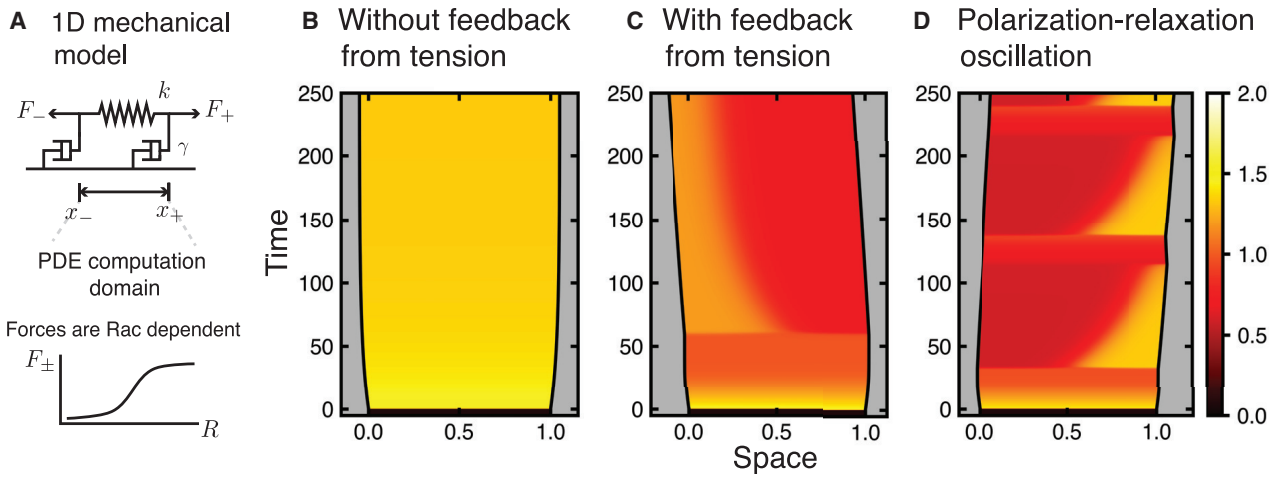

FIGURE 4 1D mechanochemical model and tension-mediated cell polarization. (*A*) The cell is modeled as a 1D elastic spring (spring constant k) and viscous damping (damping constant γ). The PDEs are solved in the domain $\Omega(t) = [x_-(t), x_+(t)]$, which varies over time because of forces $F_\pm$ that depend on Rac activity at the cell ends ($x_\pm(t)$). (*B*) Uniform stimulation leads to cell expansion without feedback from tension $\delta_1 = 0$. Black lines show $x_-(t)$ and $x_+(t)$, and color shows Rac activity. For this simulation, the cell is initialized at rest at time $t = -5$. The basal-activation rate parameter jumps from $b = 0.1$ to $b = 4$ at time $t \geq 0$. Tension feeds back onto inactivation according to $\delta(T) = \delta_0 + \delta_1 T$, $T = L(t) - \ell_0$, $\delta_0 = 3$, and $\ell_0 = 1$. Other parameters are $f_R = 0.001$, $s_1 = 10$, $s_0 = 1$, $\gamma = 1$, $k = 0.01$, $c = 5$, $n = 6$, $R_T = 2$, $D = 0.01$, and $D_{i\underline{i}} = 10$. The initial conditions are $R(x, 0) = 0.05645$ and $R_i(x, 0) = R_T - 0.05645$. See Video S2. (*C*) Uniform stimulation leads to cell expansion and polarization with feedback from tension $\delta_1 = 80$. Other parameters are as in (*B*). See Video S3. (*D*) With $b = 2$, uniform stimulation leads to indicate cyclical phases of polarization and relaxation. Other parameters and initial conditions are as in (*C*). See Video S4. To see this figure in color, go online.

The third simulation (Fig. 4 *D*) illustrates a different type of dynamic that occurs at lower levels of stimulation. Here, the cell undergoes oscillatory phases of polarized protrusion followed by loss of polarity and relaxation. In this case, the levels of stimulation are not sufficiently high to maintain polarization when tension-mediated inactivation increases. We note that this polarization-relaxation oscillation may be a consequence of the lack of explicit contractile signaling along with the simplified nature of cellular mechanics used in this model and is not observed in neutrophil stimulation experiments (to our knowledge). However, such length oscillations are observed in amoeboid cells during stepping motility (75). Thus, although we include it here for completeness, it is not the focus of this study.

Bifurcation and parameter space analysis

To supplement our proof of concept example simulations in Figs. 3 and 4, we next sought to understand the relationship between cell length changes, chemoattractant levels in the environment (modeled by the parameter b), and the resulting cell behaviors: polarized, polarization-relaxation oscillation, and nonpolarized. First, we used LPA on this system in which length is itself a parameter. In this approach, length affects the model in two ways: 1) it controls tension and 2) leads concentration or dilution effects resulting from a fixed total amount of GTPase being distributed on a smaller or larger cell surface area.

We used LPA to map the cell behavior in the bL plane (Fig. 5 *A*). Results demonstrate that the cell can exist in either a nonpolar state, stimulus-induced polarized state, or in a linearly unstable regime in which polarization results from noise (Turing regime), depending on this cell length, L, and the given basal-activation rate, b. Using this result, we can now map the dynamics of the deforming 1D model in terms of length rather than δ.

In Fig. 5 *A*, we superimpose the length variations of the simulated 1D cell onto the bifurcation diagram in the bL plane. We simulated several 1D deforming cells with different values of b (exactly as in Fig. 4, *B* and *C*). Fig. 5 *A* illustrates the trajectories of these in length-space as gray and black trajectories. Gray indicates that the cell is apolar at that point in the trajectory, whereas black indicates polarity. For small b-values (region I), the Rac activity remains sufficiently low that the cell's length does not change, and the cell remains nonpolar. For intermediate b-values (region II), the Rac activity is sufficient to induce length changes, resulting in Rac polarization. However, there is sufficient Rac activity to increase the cell length beyond the Turing regime, and polarization is lost so that the cell relaxes. When the length returns to the Turing regime, spontaneous polarization reoccurs, and the cell again lengthens, inducing a polarization-relaxation oscillation (as shown in Fig. 4 *C*). Quantification of cell length and level of polarity (*top* and *bottom panels*, respectively, of Fig. 5 *B*) further illustrate the link between polarized growth and apolar relaxation. For larger intermediate values of b (region III), the cell lengthens, and polarization persists. In this case, the length increases monotonically before approaching a constant value, with a persistent polarity. Finally, for large

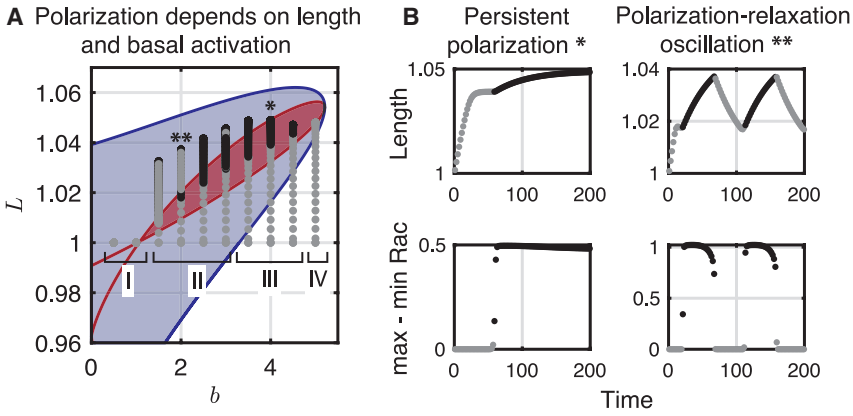

FIGURE 5 Analysis of length dependence of dynamics. (*A*) LPA of the fixed domain system (L is thus a parameter, not a variable) reveals regimes of nonpolar (*unshaded*), stimulus-induced polarization (*blue shaded region*), and Turing instability (i.e., polarizable; *inside the red shaded region*) in the bL plane. Gray and black points illustrate length L trajectories from PDE simulations for various b-values. As the length changes because of Rac activity (dependent on mechanical parameters), the cell can be in a polarized (*black*) or nonpolar (*gray*) state. Once the cell's length is in the Turing regime, polarization may occur. Regions I–IV denote the characteristic behavior for a range of b-values: I nonpolar, resting cells; II polarization-relaxation oscillation; III persistent polarization; and IV nonpolar, expanded cells. (*B*) Given are the plots of cell length (*top row*) and polarity strength (*bottom row*) for two example simulations of the coupled model in regimes III ($b = 4$; *left column*, *labeled* * in *A*) and II ($b = 2$; *right column*, *labeled* ** in *A*), respectively. Top row: shown is the length as a function of time. Bottom row: shown is the difference between maximal and minimal Rac activity as a function of time (a proxy for polarization). Color indicates polar (*black*) or nonpolar (*gray*) Rac activity. To see this figure in color, go online.

b-values (region IV), stimulation is too strong for polarity to occur. Cells in this region remain nonpolar and expanded. We do note that receptor saturation or other factors could limit the maximal level of b because Rac activation is downstream of a receptor-mediated signaling cascade. Thus, if the maximal level of receptor signaling is limited, it is possible that no level of external stimulation would perpetually overstimulate the cell.

Verification of the mechanosensing-adaptation hypothesis in a 2D continuum mechanics model

Using the 2D mechanochemical model, we repeated the simulation depicted by the arrows in Fig. 3 *A* and shown using the 1D model in Fig. 4. In Fig. 6, we perform the same simulation experiment in which an initially at rest, circular cell is uniformly stimulated with high levels of chemoattractant. As in the 1D model, if there is no feedback from tension ($\delta_1 = 0$; Fig. 6 *A*), the cell simply expands because of the uniformly increased Rac activity (*dashed line* indicates the cell's initial position). Note that there is slight movement in the positive x-direction because we apply a small gradient of the parameter b to each cell to ensure the cells consistently polarize in the same direction. With feedback from tension ($\delta_1 = 30$; Fig. 6 *B*), the cell initially expands isotropically to a point, polarizes, and then migrates. In Fig. S5, we illustrate that polarization occurs because of an increase in area to about $A \approx 1.1$ caused by increased Rac activity. We also observe the polarization-relaxation oscillation found in the 1D model for lower basal-activation rate $b = 2$ (Fig. 6 *C*); however, in 2D, we used $\delta_1 = 160$ instead of $\delta_1 = 80$ as in the 1D model. For these parameters, the polarization-relaxation oscillation is transiently present but not stable. As the cell elongates, polarization persists but oscillates in magnitude (see Video S7). These results confirm that tension-signaling feedback still leads to adaptive polarization when embedded in a 2D geometry.

Mechanosensing adaptation in a chemoattractant gradient

Thus far, we have demonstrated that tension-mediated inhibition can facilitate polarization at higher, uniform stimulation levels than are possible without it. Based on this, we hypothesize that tension will allow cells to migrate further up a stimulus gradient because they are exposed to higher and higher signaling as they migrate up a gradient.

To test this, we simulated the 1D and 2D mechanochemical models in a chemoattractant gradient encoded in a spatial gradient of the activation parameter b. We simulated 1D cells with the same parameters as in Fig. 4 for a range of feedback strengths δ_1. Each cell is subjected to a chemoattractant gradient encoded in a spatially varying basal-activation rate $b(x) = b_0 + b_2 x$. 1D simulation results show that feedback from tension ($\delta_1 > 0$) enables cells to migrate further up this gradient (Figs. 7 *A* and S5 *A*). We simulated 2D cells in the same gradient as in 1D with parameters as in Fig. 6. The cell with feedback from tension ($\delta_1 = 30$; Figs. 7 *B* and S5 *B*) migrates further as expected based on the 1D results. Together, these results suggest that feedback from tension does enable further migration and that the cell's with stronger feedback from tension (larger δ_1) migrate further than cells without feedback. In cells with stronger feedback, we observe that polarized Rac activity persists for longer than in those with weaker or without feedback (Figs. S5–S7). We do note that this is not a form of "perfect" adaptation. Eventually, all cells with this mechanism saturate their signaling and halt migration. Thus, although this form of adaptation is a natural consequence of tension inhibition,

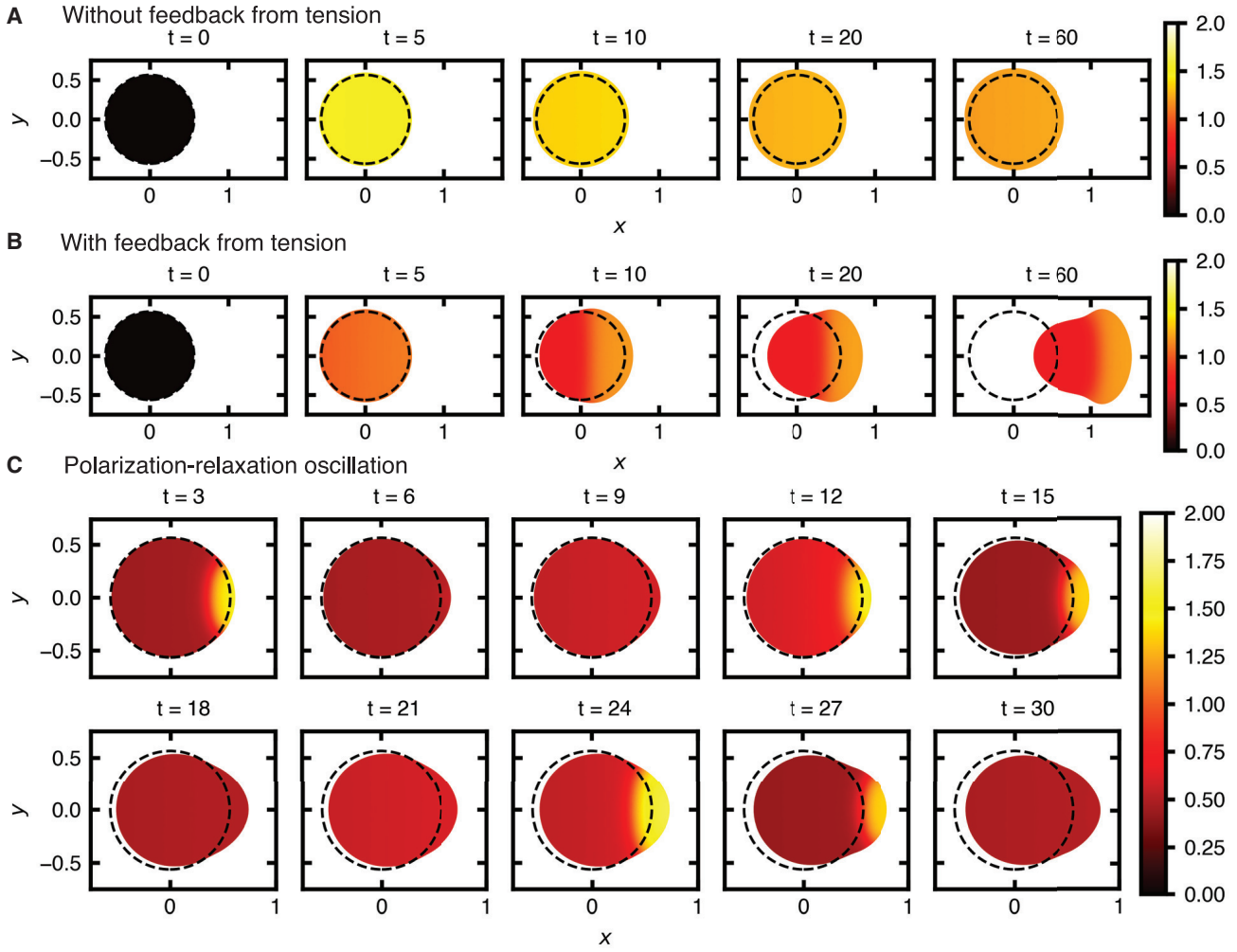

FIGURE 6 Cell polarization in the 2D mechanochemical model. (*A*) Uniform stimulation leads to cell expansion without feedback from tension $\delta_1 = 0$. The dashed line indicates the cell's initial position, and color corresponds to Rac activity. Here, δ depends on T as before: $\delta(T) = \delta_0 + \delta_1 T$; but tension is defined as the difference between this area and the rest area: $T = A(t) - A_0$ with $\delta_0 = 2$ and $A_0 = 1$. We apply a small internal chemoattractant gradient in the reference domain (i.e., in $\bar{\mathbf{x}}$-coordinates) to ensure polarization along the x-axis according to $b(\bar{\mathbf{x}}) = b_0 + b_1\bar{\mathbf{x}}$, with $b_0 = 4$ and $b_1 = 0.1$. The mechanical parameters are $f_R = 0.3$ nN/μm, $E = 0.3$ kPa, $\nu = 0.45$, $\gamma = 20$ kPa•s/μm^2, and $\beta = 10$ s. The initial conditions are $R(x, t) = 0$, $R_i(x, 0) = 2$, with the mechanical system at rest (no displacement). See Video S5. (*B*) The cell is resting when exposed to chemoattractant at $t = 0$; it first expands uniformly and subsequently polarizes and migrates because of increased feedback from tension $\delta_1 = 30$. Other parameters are as in (*A*). See Video S6. (*C*) Shown is the predicted oscillatory behavior when not oversaturated with $b_0 = 2.0$ and $\delta_1 = 160$. Other parameters are as in (*A*). See Video S7. See Fig. S5 for plots of cell area and polarity over time. To see this figure in color, go online.

we are not proposing it as a replacement for known forms of biochemical adaptation.

DISCUSSION

In this study, we coupled a reaction-diffusion model of Rac dynamics to a minimal model of cell mechanics to illustrate that the two-way feedback from membrane tension to Rac activity allows cells such as human neutrophils to adapt to saturating levels of chemoattractive environment and maintain cell polarity. We first used the LPA to map the parameter regimes of behavior of the wave-pinning model with respect to the basal activation (b, which is altered by stimulation) and deactivation rates (δ, which is altered by tension). Given the shape of polarizable region in the $b\delta$ plane, we hypothesized that an increase in the basal activation that pushes the cell into an overactivated state can be counterbalanced by a commensurate increase in the deactivation rate δ arising from increases in cell tension resulting from protrusion. We then simulated the cell's response to stimulation from uniformly high levels and a gradient of chemoattractant using 1D and 2D deformable cell models in which signaling influences cell size and tension and vice versa. Results confirmed that the interaction between tension and signaling can lead to polarization adaptation to high signaling levels and that cells with feedback from

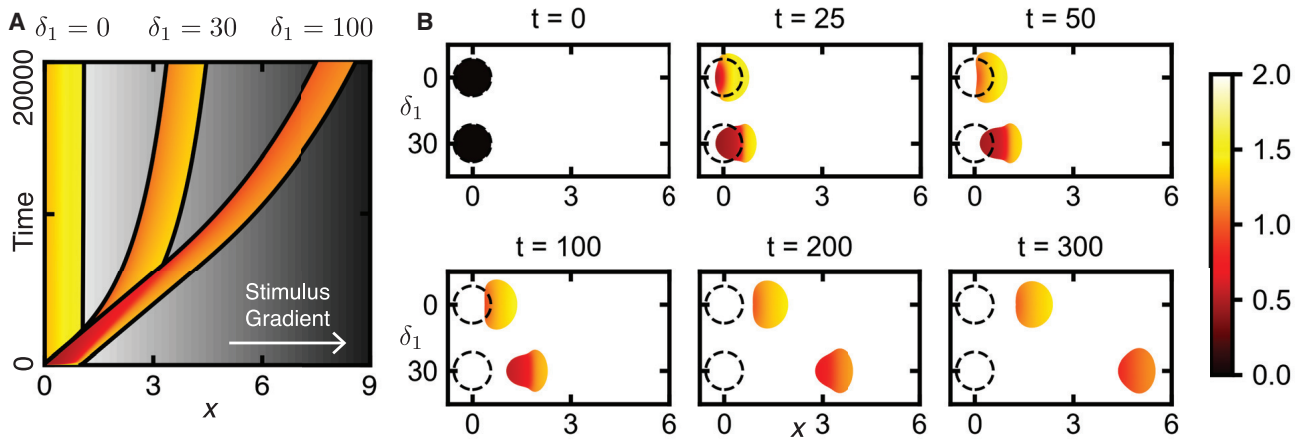

FIGURE 7 Mechanosensing adaptation enables persistent migration in a chemoattractant gradient. Cells migrate up a chemoattractant gradient encoded in the basal-activation rate $b(x) = b_0 + b_2 x$ with $b_0 = 2.5$ and $b_2 = 1$. (*A*) 1D cells with feedback from tension ($\delta_1 > 0$) are able to migrate further up the chemoattractant gradient than those without feedback from tension ($\delta_1 = 0$) before becoming overstimulated and losing polarity (see also Figs. S5 *A* and S6). (*B*) Snapshots over time of migrating cells in 2D without (*top cell*; $\delta_1 = 0$) and with (*bottom cell*; $\delta_1 = 30$) feedback from tension reveal the same behavior as in 1D (see also Fig. S7 *B*). Shown are parameters as in Fig. 6, *A* and *B* except there is no longer an internal gradient applied to the interior of the cell in the stationary domain ($b_1 = 0$). The dashed circle shows the initial position. See Videos S8 and S9. Color shows Rac activity in all panels. To see this figure in color, go online.

tension can migrate further up a chemoattractant gradient before becoming oversaturated and losing polarity. We coupled the LPA with these full model simulations to demonstrate that the adaptive polarity that arises after uniform stimulation is the result of the cell passing through a bifurcation in the GTPase system. Thus, cell area changes that result from overstimulation force the cell back into a polarizable state by counterbalancing that stimulation. These results broadly support the hypothesis that mechanosensing can act as an adaptive response to maintain polarity in migrating cells. Further, they are consistent with the conclusions of experimental observations connecting cell mechanics and cell signaling (3–5).

Our study makes several testable predictions. First, our model predicts a relationship between polarity, tension, and cell area. Measurements of cell polarity, tension, and cell area during neutrophil stimulation experiments could be jointly plotted to test the presence of such a relationship. Fluorescent probes or downstream readouts can be used to assess Rac activity levels during neutrophil stimulation experiments (3,41), whereas the optical trap force measurements can measure tension (76). Second, to test whether tension plays a role in the adaptive response, the neutrophil stimulation experiment could be performed on cells with inhibited actin-based protrusion. If tension is responsible for the adaptive response, the hypothesis would be that in the absence of protrusion, uniform signaling activation would occur and persist instead of polarization (though it is possible the formation of blebs (41) or some other unintended effect could complicate matters). Such cells (with and without feedback from tension) could also be exposed to chemoattractant gradients as in Fig. 7 to assess whether tension enables persistent migration. Third, at lower levels of chemoattractant stimulation, the simulated cells oscillate between a polarized and relaxed state. Although such length oscillations are observed during stepping motility in amoeboid cells (75), to our knowledge, they are not observed in uniformly stimulated neutrophils.

Numerous studies have used differing computational approaches to study the consequences of mechanics, geometry, and tension on cell dynamics, such as explicitly modeling the competition between separate front and rear cellular compartments (77,78), phase-field simulations incorporating feedback from tension, and other physical parameters (46,47,49,51,54,55), cellular Potts model simulations (53,79,80), level-set methods (81–83), immersed-boundary models (45,84,85), free-boundary models (48,86), or stochastic methods (50,87). Our work differs from these numerous prior studies in that we study how the interplay between mechanics and signaling facilitates adaptation. In this sense, our work is most similar to that of Buttenschön et al. (64), who considered the wave-pinning model coupled to a similar 1D mechanical model. Their work did not, however, incorporate feedback from mechanics to signaling. Zmurchok et al. (88) investigated the consequences of this feedback. However, because this study was primarily concerned with collective, multicellular dynamics, each cell was treated as a well-mixed point entity (i.e., polarity was not possible), and adaptation was not studied. Kopfer et al. (89) coupled a model of GTPase kinetics with actin and myosin dynamics along with a viscous active gel model for cellular physics (opposite our continuum mechanics model). Their results, however, primarily focused on demonstrating the ability of tension to limit protrusion to a single front

and resolve conflicting stimuli. Thus, although our mechano-chemical modeling fits into this larger body of literature, the intent and results, namely to demonstrate the adaptive nature of tension-mediated mechanochemical feedback, are distinct.

This study does have limitations. We chose to allow cell mechanics to affect the deactivation rate (δ). This is likely an oversimplification. It is possible that tension could influence activation in an inverse way, though this would likely lead to similar qualitative results. We also chose to study the simplest model for Rac signaling and did not explore more complicated variants that include multiple GTPases (26,31,33) or additional feedback networks (80). This was motivated by both simplicity and the fact that the interaction between Rac and tension has been well studied experimentally (3–5). We also defined cell tension as a global quantity despite evidence suggesting that membrane tension is more localized than previously thought (76) and that cells such as keratocytes generate tension gradients (90,91). In our study, however, we are concerned primarily with how cells respond to uniformly high stimulation that would be expected to, broadly speaking, lead to global increases in tension due to protrusion. Lastly, we used the simplest mechanical models appropriate for cell mechanics (an overdamped elastic spring in 1D and linear viscoelasticity in 2D) and approximate estimates of biochemical and biophysical parameters. Although this is sufficient for our purpose, a more detailed model of cell mechanics and/or precisely measured or estimated biophysical parameter values would be required to study 2D migration itself (as has been done by many others (44–53,55)).

Despite these limitations, this study demonstrates that mechanosensing can act as an adaptive response to maintain polarity in environments with high levels of chemoattractant. We confirm that the feedback for establishment of polarity via membrane tension can be described using a wave-pinning model of Rac signaling. Although we have assumed that membrane tension is a global quantity that feeds back into Rac signaling dynamics, we note that the underlying signaling network is responsible for the adaptive response. Any signal that acts on Rac dynamics in a similar way could induce a similar response (calcium influx, for example, as suggested by Shi et al. (76)). This type of mechano-chemical adaptation is a potential alternative that may work in parallel to biochemical mechanisms of adaptation.

Data availability

The code used to produce the 1D simulations is available as an archived GitHub repository at https://doi.org/10.6084/m9.figshare.11916495. The code for the 2D simulations can be made available upon request.

SUPPORTING MATERIAL

Supporting Material can be found online at https://doi.org/10.1016/j.bpj.2020.08.035.

AUTHOR CONTRIBUTIONS

C.Z. and W.R.H. designed the research. C.Z. and J.C. performed the research and analyzed the data. All authors wrote the article.

ACKNOWLEDGMENTS

The authors acknowledge Christopher Bradley for helpful discussions on numerical implementation of the coupled mechanics and reaction-diffusion simulations and Andreas Buttenschön for helpful discussions of the 1D model.

This work was supported by a National Science Foundation, United States, grant DMS1562078 (to W.R.H.) and a Natural Sciences and Engineering Research Council of Canada Postdoctoral Fellowship Award (to C.Z.).

SUPPORTING CITATIONS

Reference (92) appears in the Supporting Material.

REFERENCES

1. Zigmond, S. H. 1974. Mechanisms of sensing chemical gradients by polymorphonuclear leukocytes. *Nature.* 249:450–452.
2. Gardiner, E. M., K. N. Pestonjamasp, …, G. M. Bokoch. 2002. Spatial and temporal analysis of Rac activation during live neutrophil chemotaxis. *Curr. Biol.* 12:2029–2034.
3. Weiner, O. D., W. A. Marganski, …, M. W. Kirschner. 2007. An actin-based wave generator organizes cell motility. *PLoS Biol.* 5:e221.
4. Houk, A. R., A. Jilkine, …, O. D. Weiner. 2012. Membrane tension maintains cell polarity by confining signals to the leading edge during neutrophil migration. *Cell.* 148:175–188.
5. Saha, S., T. L. Nagy, and O. D. Weiner. 2018. Joining forces: crosstalk between biochemical signalling and physical forces orchestrates cellular polarity and dynamics. *Philos. Trans. R Soc. Lond. B Biol. Sci.* 373:20170145.
6. Spiro, P. A., J. S. Parkinson, and H. G. Othmer. 1997. A model of excitation and adaptation in bacterial chemotaxis. *Proc. Natl. Acad. Sci. USA.* 94:7263–7268.
7. Barkai, N., and S. Leibler. 1997. Robustness in simple biochemical networks. *Nature.* 387:913–917.
8. Koshland, D. E., Jr. 1977. A response regulator model in a simple sensory system. *Science.* 196:1055–1063.
9. Iglesias, P. A., and C. Shi. 2014. Comparison of adaptation motifs: temporal, stochastic and spatial responses. *IET Syst. Biol.* 8:268–281.
10. Meinhardt, H. 1999. Orientation of chemotactic cells and growth cones: models and mechanisms. *J. Cell Sci.* 112:2867–2874.
11. Parent, C. A., and P. N. Devreotes. 1999. A cell's sense of direction. *Science.* 284:765–770.
12. Levchenko, A., and P. A. Iglesias. 2002. Models of eukaryotic gradient sensing: application to chemotaxis of amoebae and neutrophils. *Biophys. J.* 82:50–63.
13. Ma, L., C. Janetopoulos, …, P. A. Iglesias. 2004. Two complementary, local excitation, global inhibition mechanisms acting in parallel can explain the chemoattractant-induced regulation of PI(3,4,5)P3 response in dictyostelium cells. *Biophys. J.* 87:3764–3774.
14. Levine, H., D. A. Kessler, and W. J. Rappel. 2006. Directional sensing in eukaryotic chemotaxis: a balanced inactivation model. *Proc. Natl. Acad. Sci. USA.* 103:9761–9766.
15. Iglesias, P. A., and P. N. Devreotes. 2008. Navigating through models of chemotaxis. *Curr. Opin. Cell Biol.* 20:35–40.

16. Xiong, Y., C. H. Huang, …, P. N. Devreotes. 2010. Cells navigate with a local-excitation, global-inhibition-biased excitable network. *Proc. Natl. Acad. Sci. USA.* 107:17079–17086.

17. Iglesias, P. A., and P. N. Devreotes. 2012. Biased excitable networks: how cells direct motion in response to gradients. *Curr. Opin. Cell Biol.* 24:245–253.

18. Wang, M. J., Y. Artemenko, …, P. N. Devreotes. 2014. The directional response of chemotactic cells depends on a balance between cytoskeletal architecture and the external gradient. *Cell Rep.* 9:1110–1121.

19. Devreotes, P. N., S. Bhattacharya, …, Y. Miao. 2017. Excitable signal transduction networks in directed cell migration. *Annu. Rev. Cell Dev. Biol.* 33:103–125.

20. Matthews, B. D., D. R. Overby, …, D. E. Ingber. 2006. Cellular adaptation to mechanical stress: role of integrins, Rho, cytoskeletal tension and mechanosensitive ion channels. *J. Cell Sci.* 119:508–518.

21. Trichet, L., J. Le Digabel, …, B. Ladoux. 2012. Evidence of a large-scale mechanosensing mechanism for cellular adaptation to substrate stiffness. *Proc. Natl. Acad. Sci. USA.* 109:6933–6938.

22. Rappel, W. J., and L. Edelstein-Keshet. 2017. Mechanisms of cell polarization. *Curr. Opin. Syst. Biol.* 3:43–53.

23. Ridley, A. J. 2015. Rho GTPase signalling in cell migration. *Curr. Opin. Cell Biol.* 36:103–112.

24. Mori, Y., A. Jilkine, and L. Edelstein-Keshet. 2008. Wave-pinning and cell polarity from a bistable reaction-diffusion system. *Biophys. J.* 94:3684–3697.

25. Mori, Y., A. Jilkine, and L. Edelstein-Keshet. 2011. Asymptotic and bifurcation analysis of wave-pinning in a reaction-diffusion model for cell polarization. *SIAM J. Appl. Math.* 71:1401–1427.

26. Jilkine, A., A. F. M. Marée, and L. Edelstein-Keshet. 2007. Mathematical model for spatial segregation of the Rho-family GTPases based on inhibitory crosstalk. *Bull. Math. Biol.* 69:1943–1978.

27. Holmes, W. R., A. E. Carlsson, and L. Edelstein-Keshet. 2012. Regimes of wave type patterning driven by refractory actin feedback: transition from static polarization to dynamic wave behaviour. *Phys. Biol.* 9:046005.

28. Rajagopal, V., W. R. Holmes, and P. V. S. Lee. 2018. Computational modeling of single-cell mechanics and cytoskeletal mechanobiology. *Wiley Interdiscip. Rev. Syst. Biol. Med.* 10:e1407.

29. Edelstein-Keshet, L., W. R. Holmes, …, M. Dutot. 2013. From simple to detailed models for cell polarization. *Philos. Trans. R. Soc. Lond. B Biol. Sci.* 368:20130003.

30. Holmes, W. R., L. Liao, …, L. Edelstein-Keshet. 2015. Modeling the roles of protein kinase Cβ and η in single-cell wound repair. *Mol. Biol. Cell.* 26:4100–4108.

31. Holmes, W. R., and L. Edelstein-Keshet. 2016. Analysis of a minimal Rho-GTPase circuit regulating cell shape. *Phys. Biol.* 13:046001.

32. Holmes, W. R., A. E. Golding, …, L. Edelstein-Keshet. 2016. A mathematical model of GTPase pattern formation during single-cell wound repair. *Interface Focus.* 6:20160032.

33. Zmurchok, C., and W. R. Holmes. 2020. Simple rho GTPase dynamics generate a complex regulatory landscape associated with cell shape. *Biophys. J.* 118:1438–1454.

34. Katsumi, A., J. Milanini, …, M. A. Schwartz. 2002. Effects of cell tension on the small GTPase Rac. *J. Cell Biol.* 158:153–164.

35. Gauthier, N. C., T. A. Masters, and M. P. Sheetz. 2012. Mechanical feedback between membrane tension and dynamics. *Trends Cell Biol.* 22:527–535.

36. Lessey, E. C., C. Guilluy, and K. Burridge. 2012. From mechanical force to RhoA activation. *Biochemistry.* 51:7420–7432.

37. Masters, T. A., B. Pontes, …, N. C. Gauthier. 2013. Plasma membrane tension orchestrates membrane trafficking, cytoskeletal remodeling, and biochemical signaling during phagocytosis. *Proc. Natl. Acad. Sci. USA.* 110:11875–11880.

38. Tao, J., and S. X. Sun. 2015. Active biochemical regulation of cell volume and a simple model of cell tension response. *Biophys. J.* 109:1541–1550.

39. Scott, D. W., C. E. Tolbert, and K. Burridge. 2016. Tension on JAM-A activates RhoA via GEF-H1 and p115 RhoGEF. *Mol. Biol. Cell.* 27:1420–1430.

40. He, L., J. Tao, …, S. X. Sun. 2018. Role of membrane-tension gated Ca^{2+} flux in cell mechanosensation. *J. Cell Sci.* 131:jcs208470.

41. Graziano, B. R., J. P. Town, …, O. D. Weiner. 2019. Cell confinement reveals a branched-actin independent circuit for neutrophil polarity. *PLoS Biol.* 17:e3000457.

42. Holmes, W. R. 2014. An efficient, nonlinear stability analysis for detecting pattern formation in reaction diffusion systems. *Bull. Math. Biol.* 76:157–183.

43. Holmes, W. R., M. A. Mata, and L. Edelstein-Keshet. 2015. Local perturbation analysis: a computational tool for biophysical reaction-diffusion models. *Biophys. J.* 108:230–236.

44. Holmes, W. R., and L. Edelstein-Keshet. 2012. A comparison of computational models for eukaryotic cell shape and motility. *PLoS Comput. Biol.* 8:e1002793.

45. Wu, T., and J. J. Feng. 2015. Modeling the mechanosensitivity of neutrophils passing through a narrow channel. *Biophys. J.* 109:2235–2245.

46. Winkler, B., I. S. Aranson, and F. Ziebert. 2016. Membrane tension feedback on shape and motility of eukaryotic cells. *Physica D.* 318–319:26–33.

47. Camley, B. A., Y. Zhao, …, W. J. Rappel. 2017. Crawling and turning in a minimal reaction-diffusion cell motility model: coupling cell shape and biochemistry. *Phys. Rev. E.* 95:012401.

48. Nickaeen, M., I. L. Novak, …, B. M. Slepchenko. 2017. A free-boundary model of a motile cell explains turning behavior. *PLoS Comput. Biol.* 13:e1005862.

49. Wang, W., K. Tao, …, F. Liu. 2017. Exploring the inhibitory effect of membrane tension on cell polarization. *PLoS Comput. Biol.* 13:e1005354.

50. Trogdon, M., B. Drawert, …, L. R. Petzold. 2018. The effect of cell geometry on polarization in budding yeast. *PLoS Comput. Biol.* 14:e1006241.

51. Cao, Y., E. Ghabache, and W. J. Rappel. 2019. Plasticity of cell migration resulting from mechanochemical coupling. *eLife.* 8:e48478.

52. Marzban, B., J. Kang, …, H. Yuan. 2019. A contraction–reaction–diffusion model: integrating biomechanics and biochemistry in cell migration. *Extreme Mech. Lett.* 32:100566.

53. Rens, E. G., and L. Edelstein-Keshet. 2019. From energy to cellular forces in the Cellular Potts Model: an algorithmic approach. *PLoS Comput. Biol.* 15:e1007459.

54. Cao, Y., E. Ghabache, …, W. J. Rappel. 2019. A minimal computational model for three-dimensional cell migration. *J. R. Soc. Interface.* 16:20190619.

55. Tao, K., J. Wang, …, L. Zhang. 2020. Tuning cell motility via cell tension with a mechanochemical cell migration model. *Biophys. J.* 118:2894–2904.

56. Walther, G. R., A. F. M. Marée, …, V. A. Grieneisen. 2012. Deterministic versus stochastic cell polarisation through wave-pinning. *Bull. Math. Biol.* 74:2570–2599.

57. Mata, M. A., M. Dutot, …, W. R. Holmes. 2013. A model for intracellular actin waves explored by nonlinear local perturbation analysis. *J. Theor. Biol.* 334:149–161.

58. Nakamura, N., and T. Shibata. 2015. Bifurcation analysis of a self-organizing signaling system for eukaryotic chemotaxis. *Jpn. J. Ind. Appl. Math.* 32:807–828.

59. Jacobs, B., J. Molenaar, and E. E. Deinum. 2019. Small GTPase patterning: how to stabilise cluster coexistence. *PLoS One.* 14:e0213188.

60. Liu, Y., E. G. Rens, and L. Edelstein-Keshet. 2019. Spots, strips, and spiral waves in models for static and motile cells. *arXiv*, arXiv:1909.10504.

61. Crampin, E. J., E. A. Gaffney, and P. K. Maini. 1999. Reaction and diffusion on growing domains: scenarios for robust pattern formation. *Bull. Math. Biol.* 61:1093–1120.

62. Crampin, E. J., W. W. Hackborn, and P. K. Maini. 2002. Pattern formation in reaction-diffusion models with nonuniform domain growth. *Bull. Math. Biol.* 64:747–769.

63. Baker, R. E., and P. K. Maini. 2007. A mechanism for morphogen-controlled domain growth. *J. Math. Biol.* 54:597–622.

64. Buttenschön, A., Y. Liu, and L. Edelstein-Keshet. 2020. Cell size, mechanical tension, and GTPase signaling in the single cell. *Bull. Math. Biol.* 82:28.

65. Jones, E., T. Oliphant, and P. Peterson. 2001. SciPy: open source scientific tools for Python. *SciPy* http://www.scipy.org/.

66. Hindmarsh, A. C. 1983. ODEPACK, a systematized collection of ODE solvers. *In* Scientific Computing. R. S. Stepleman, M. Carver, R. Peskin, W. F. Ames, and R. Vichnevetsky, eds. North-Holland Publishing Company.

67. Petzold, L. 1983. Automatic selection of methods for solving stiff and nonstiff systems of ordinary differential equations. *SIAM J. Sci. Statist. Comput.* 4:136–148.

68. Hunter, J. D. 2007. Matplotlib: a 2D graphics environment. *Comput. Sci. Eng.* 9:90–95.

69. Alnæs, M., J. Blechta, …, A. Logg. 2015. The FEniCS project version 1.5. Archive of Numerical Software. https://doi.org/10.11588/ans.2015.100.20553.

70. Armistead, F. J., J. Gala De Pablo, …, S. D. Evans. 2019. Cells under stress: an inertial-shear microfluidic determination of cell behavior. *Biophys. J.* 116:1127–1135.

71. Hauert, A. B., S. Martinelli, …, V. Niggli. 2002. Differentiated HL-60 cells are a valid model system for the analysis of human neutrophil migration and chemotaxis. *Int. J. Biochem. Cell Biol.* 34:838–854.

72. Bausch, A. R., F. Ziemann, …, E. Sackmann. 1998. Local measurements of viscoelastic parameters of adherent cell surfaces by magnetic bead microrheometry. *Biophys. J.* 75:2038–2049.

73. Mogilner, A., and G. Oster. 2003. Force generation by actin polymerization II: the elastic ratchet and tethered filaments. *Biophys. J.* 84:1591–1605.

74. Hoang, A. N., C. N. Jones, …, D. Irimia. 2013. Measuring neutrophil speed and directionality during chemotaxis, directly from a droplet of whole blood. *Technology (Singap World Sci).* 1:49–57.

75. Copos, C. A., S. Walcott, …, R. D. Guy. 2017. Mechanosensitive adhesion explains stepping motility in amoeboid cells. *Biophys. J.* 112:2672–2682.

76. Shi, Z., Z. T. Graber, …, A. E. Cohen. 2018. Cell membranes resist flow. *Cell.* 175:1769–1779.e13.

77. Holmes, W. R., J. Park, …, L. Edelstein-Keshet. 2017. A mathematical model coupling polarity signaling to cell adhesion explains diverse cell migration patterns. *PLoS Comput. Biol.* 13:e1005524.

78. Park, J., W. R. Holmes, …, A. Levchenko. 2017. Mechanochemical feedback underlies coexistence of qualitatively distinct cell polarity patterns within diverse cell populations. *Proc. Natl. Acad. Sci. USA.* 114:E5750–E5759.

79. Marée, A. F. M., A. Jilkine, …, L. Edelstein-Keshet. 2006. Polarization and movement of keratocytes: a multiscale modelling approach. *Bull. Math. Biol.* 68:1169–1211.

80. Marée, A. F. M., V. A. Grieneisen, and L. Edelstein-Keshet. 2012. How cells integrate complex stimuli: the effect of feedback from phosphoinositides and cell shape on cell polarization and motility. *PLoS Comput. Biol.* 8:e1002402.

81. Wolgemuth, C. W., and M. Zajac. 2010. The Moving Boundary Node Method: a level set-based, finite volume algorithm with applications to cell motility. *J. Comput. Phys.* 229:7287–7308.

82. Neilson, M. P., D. M. Veltman, …, R. H. Insall. 2011. Chemotaxis: a feedback-based computational model robustly predicts multiple aspects of real cell behaviour. *PLoS Biol.* 9:e1000618.

83. Shi, C., C. H. Huang, …, P. A. Iglesias. 2013. Interaction of motility, directional sensing, and polarity modules recreates the behaviors of chemotaxing cells. *PLoS Comput. Biol.* 9:e1003122.

84. Vanderlei, B., J. J. Feng, and L. Edelstein-Keshet. 2011. A computational model of cell polarization and motility coupling mechanics and biochemistry. *Multiscale Model. Simul.* 9:1420–1443.

85. Strychalski, W., C. A. Copos, …, R. D. Guy. 2015. A poroelastic immersed boundary method with applications to cell biology. *J. Comput. Phys.* 282:77–97.

86. Rubinstein, B., K. Jacobson, and A. Mogilner. 2005. Multiscale two-dimensional modeling of a motile simple-shaped cell. *Multiscale Model. Simul.* 3:413–439.

87. Copos, C., and A. Mogilner. 2020. A hybrid stochastic-deterministic mechanochemical model of cell polarization. *Mol. Biol. Cell.* 31:1637–1649.

88. Zmurchok, C., D. Bhaskar, and L. Edelstein-Keshet. 2018. Coupling mechanical tension and GTPase signaling to generate cell and tissue dynamics. *Phys. Biol.* 15:046004.

89. Kopfer, K. H., W. Jäger, and F. Matthäus. 2020. A mechanochemical model for rho GTPase mediated cell polarization. *J. Theor. Biol.* 504:110386.

90. Lieber, A. D., Y. Schweitzer, …, K. Keren. 2015. Front-to-rear membrane tension gradient in rapidly moving cells. *Biophys. J.* 108:1599–1603.

91. Fogelson, B., and A. Mogilner. 2014. Computational estimates of membrane flow and tension gradient in motile cells. *PLoS One.* 9:e84524.

92. Simon, C. M., E. M. Vaughan, …, L. Edelstein-Keshet. 2013. Pattern formation of Rho GTPases in single cell wound healing. *Mol. Biol. Cell.* 24:421–432.

Biophysical Journal, Volume *119*

Supplemental Information

Membrane Tension Can Enhance Adaptation to Maintain Polarity of Migrating Cells

Cole Zmurchok, Jared Collette, Vijay Rajagopal, and William R. Holmes

Supporting Material

Membrane tension can enhance adaptation to maintain polarity of migrating cells

Cole Zmurchok[1,*], Jared Collette[2,*], Vijay Rajagopal[2], William R. Holmes[1,3,4†]

[1]Department of Physics and Astronomy, Vanderbilt University, Nashville, TN, USA
[2]Department of Biomedical Engineering, University of Melbourne, Melbourne, Australia
[3]Department of Mathematics, Vanderbilt University, Nashville, TN, USA
[4]Quantitative Systems Biology Center, Vanderbilt University, Nashville, TN, USA

1 1D models

1.1 Wave-pinning model for Rac GTPase activity

We use the wave-pinning model [1] to describe Rac GTPase activity. We track the activity of active Rac ($\tilde{R}(z,\tau)$) and inactive Rac ($\tilde{R}_i(z,\tau)$) in a 1D domain $z \in [0, L_0]$ with no-flux boundary conditions ($\frac{\partial R}{\partial z} = \frac{\partial R_i}{\partial z} = 0$ for $z = 0, L_0$). The system of reaction-diffusion PDE governing the Rac dynamics are:

$$\frac{\partial \tilde{R}}{\partial \tau} = \left(\tilde{b} + \tilde{c}\frac{\tilde{R}^n}{R_0^n + \tilde{R}^n}\right)\tilde{R}_i - \delta\tilde{R} + \tilde{D}\frac{\partial^2 \tilde{R}}{\partial z^2}, \tag{1.1a}$$

$$\frac{\partial \tilde{R}_i}{\partial \tau} = -\left(\tilde{b} + \tilde{c}\frac{\tilde{R}^n}{R_0^n + \tilde{R}^n}\right)\tilde{R}_i + \delta\tilde{R} + \tilde{D}_i\frac{\partial^2 \tilde{R}_i}{\partial z^2}. \tag{1.1b}$$

Here, the activation rates (terms in parenthesis) are comprised of a basal activation rate $\tilde{b}$ and a Hill function with magnitude $\tilde{c}$, half-maximum $\tilde{R}_0$ and exponent n, modeling auto-activation, the deactivation rate is δ, and $\tilde{D}$ and $\tilde{D}_i$ are the diffusion coefficients of the active and inactive forms, respectively.

Note that we have assumed that the total amount of Rac is conserved within the cell, since Rac merely switches between active and inactive forms. Adding Equation (1.1a) to Equation (1.1b), integrating across the domain $[0, L_0]$, and using the boundary conditions gives

$$\int_0^{L_0} \tilde{R}(z,\tau) + \tilde{R}_i(z,\tau)\, dz = L_0\tilde{R}_T, \tag{1.1c}$$

where $\tilde{R}_T$ is the mean Rac concentration ($L_0\tilde{R}_T$ is the total amount of Rac). To non-dimensionalize the wave-pinning model, we introduce:

$$R = \frac{\tilde{R}}{R_0}, \quad R_i = \frac{\tilde{R}_i}{R_0}, \quad t = \tau, \quad \text{and} \quad x = \frac{z}{L_0}. \tag{1.2}$$

*co-first author
†william.holmes@vanderbilt.edu

Note that we do not scale time by the deactivation rate δ as we wish to explore the affect of δ on the system dynamics. With this scaling, the equations become

$$\frac{\partial R}{\partial t} = \left(b + c\frac{R^n}{1+R^n}\right) R_i - \delta R + D\frac{\partial^2 R}{\partial x^2}, \tag{1.3a}$$

$$\frac{\partial R_i}{\partial t} = -\left(b + c\frac{R^n}{1+R^n}\right) R_i + \delta R + D_i\frac{\partial^2 R_i}{\partial x^2}. \tag{1.3b}$$

where the scaled parameters are

$$b = \tilde{b}, \quad c = \tilde{c}, \quad , D = \frac{\tilde{D}}{L_0^2}, \quad D_i = \frac{\tilde{D}_i}{L_0^2}, \quad \text{and} \quad R_T = \frac{\tilde{R}_T}{R_0}. \tag{1.4}$$

Note also now that the conservation statement is:

$$\int_0^1 R(x,t) + R_i(x,t)\, dx = R_T. \tag{1.5}$$

1.2 Local Perturbation Analysis of the wave-pinning model

Local Perturbation Analysis (LPA) [2] is an approximation method that can be used to facilitate the prediction about the behavior of a spatial reaction-diffusion PDE model with fast and slowly diffusing variables will respond to spatially heterogeneous perturbations from homogeneous steady-states (HSS). See [3] for a detailed tutorial.

In short, by considering the evolution of an asymptotically small width static-in-time pulse-like perturbation in the slowly diffusing variables (in this case active Rac) through exploiting the fast/slow discrepancy between the quickly diffusing inactive Rac and the slowly diffusing active Rac, LPA reduces the system of PDE to a collection of more easily analyzed ODEs. These ODEs describe the evolution of concentrations of near (local variables) and away from (global variables) the perturbation on the intermediate reaction timescale. On the intermediate reaction timescale, a pulse in the slow variable will not yet be affected by the slow diffusion, but any changes to the inactive variable will be affected by the fast diffusion. Thus, away from the perturbation, the system evolves according to the well-mixed kinetics with activity levels at the homogeneous steady-state. Inside the perturbation the system will evolve due to the reaction kinetics evaluated at the global inactive Rac level $R_i = R_T - R$ and at the perturbation height R^ℓ. Applying LPA to simplify the wave-pinning model yields the following system of ODEs describing the evolution of the global R and local R^ℓ variables:

$$\frac{dR}{dt} = \left(b + c\frac{R^n}{1+R^n}\right)(R_T - R) - \delta R, \tag{1.6a}$$

$$\frac{dR^\ell}{dt} = \left(b + c\frac{(R^\ell)^n}{1+(R^\ell)^n}\right)(R_T - R) - \delta R^\ell. \tag{1.6b}$$

Note that the global variable R_i has been removed from this system due to mass conservation (here $R_i = R_T - R$).

We next used the numerical continuation package XPPAUT to perform a bifurcation analysis of the LPA system (Equation (1.6)), and to produce Figure 2A and Figure 3A. To make this diagram, we first performed a one-parameter bifurcation analysis of the LPA system with respect to the parameter b as shown in Supporting Figure 1. In this LPA bifurcation diagram, the monotonic solution branch (black curve) represents a HSS steady-state while the loop of solutions (grey curve) corresponds to non-trivial states where the local R^ℓ and global R activities differ. The presence of this local solution branch indicates

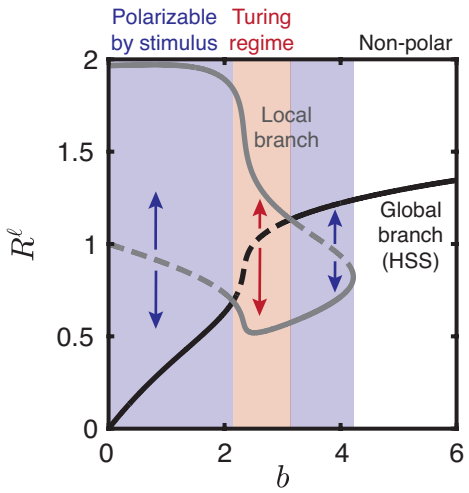

Supporting Figure 1: LPA Bifurcation Diagram. Bifurcation analysis of Equation (1.6) reveals three regimes of behavior: polarizable by stimulus (blue shaded), Turing regime (red shaded), and non-polar regime (unshaded). The local perturbation R^ℓ can attain a steady-state value different from the homogeneous steady-state (HSS) in the polarizable by stimulus region provided its amplitude differs from the HSS sufficiently. In the Turing regime, the HSS is linearly unstable to perturbations while the HSS is the only linearly stable state in the non-polar regime. Parameters are $R_T = 2$, $c = 5$, $n = 6$, and $\delta = 5$.

the potential of some spatial effect since, in these cases, the local perturbation can grow to attain a value different from the background value, possibly driving pattern formation. Bifurcation analysis of the LPA system identifies three regimes of behavior. First, for large values of b the only steady-state is the global steady-state that corresponds to a stable HSS. Second, for small and intermediate values of b we say that the system is polarizable by a stimulus (blue shaded regions) since the local perturbation can either decay back to the global HSS or grow to a different amplitude depending on its initial magnitude (blue arrows). Finally, for intermediate values of b we say that the system is in a Turing regime since in this region the HSS is linearly unstable and any perturbation will grow to the local branch.

To make the diagram in Figure 2A and Figure 3A in the paper, we first identified the saddle node bifurcations associated with the local branch that demarcate the polarizable region (at $b \approx 4.1$) and the branch points where the local solution branch bifurcates from the global solution branch (the branch points that demarcate the Turing regime). Next, we continued the saddle node bifurcations and the branch points in the $b\delta$-plane to find the curve marking the boundary of the polarizable region (blue curve) and the boundary of the linearly unstable Turing regime (red curve), respectively.

1.3 1D mechanochemical model

To couple Rac activity and cell mechanics in 1D, we solve the Rac activity PDEs in a time-dependent domain and allow this domain to change as a result of Rac activity. The model formulation and analysis is similar to other investigations of pattern-forming reaction-diffusion PDE in 1D such as [4–7]. In this formulation, we track active ($R(x,t)$) and inactive ($R_i(x,t)$) Rac activity on a time-dependent domain $\Omega(t) = [x_-(t), x_+(t)]$. We assume that the domain $\Omega(t)$ is 1D interval (initially $[0,1]$ at $t = 0$) where the boundary points depend on the displacement by the velocity field $a(x,t)$:

$$x'_-(t) = a(x_-(t),t), \quad x'_+(0) = 0, \tag{1.7a}$$

$$x'_+(t) = a(x_+(t),t), \quad x'_+(0) = 1. \tag{1.7b}$$

We assume that (1) tension affects Rac activity, (2) Rac activity affects the velocity field, and (3) tension is a global quantity that does not vary in space. Thus, we consider the following reaction-diffusion-advection model of the wave-pinning system:

$$\frac{\partial R}{\partial t} + \frac{\partial}{\partial x}(aR) = D\frac{\partial^2 R}{\partial x^2} + f(R, R_i, T), \tag{1.8a}$$

$$\frac{\partial R_i}{\partial t} + \frac{\partial}{\partial x}(aR_i) = D_i\frac{\partial^2 R_i}{\partial x^2} - f(R, R_i, T). \tag{1.8b}$$

Here, the reaction function $f(R, R_i, T)$ is modified from the standard wave-pinning model to include tension-dependent deactivation of active Rac:

$$f(R, R_i, T) = \left(b + c\frac{R^n}{R_0^n + R^n}\right) R_i - \delta(T)R, \tag{1.9}$$

where $\delta(T) = \delta_0 + \delta_1 T$ describes how tension modulates Rac deactivation. Here, tension is defined as the difference between the length and rest-length of the spring: $T = L - \ell_0$.

By treating the domain boundary as a moving discontinuity, we can use the Rakine-Hugoniot jump conditions to determine that no-flux boundary conditions are appropriate (see §1.3.2):

$$R_x = R_{ix} = 0 \quad \text{at} \quad x = x_-(t), x_+(t). \tag{1.10}$$

Given these boundary conditions, the total Rac GTPase is conserved within the cell:

$$\int_{x_-(t)}^{x_+(t)} (R + R_i)\, dx = R_T \tag{1.11}$$

for all time t. We model the cell as linear elastic spring, and that active Rac is responsible for protrusive forces on the cell ends. That is, we set

$$\gamma\frac{dx_-}{dt} = k(x_+ - x_- - \ell_0) - F_-(R(x_-(t), t)) \tag{1.12a}$$

$$\gamma\frac{dx_+}{dt} = -k(x_+ - x_- - \ell_0) + F_+(R(x_+(t), t)) \tag{1.12b}$$

where γ is the viscosity, k is the spring constant, $\ell_0 = 1$ is the rest-length and the functions $F_\pm$ describe the protrusive forces oriented outward from the cell from R. Note that inertial effects are ignored as appropriate for modeling cell motion. We use a smoothed Heaviside function for $F_\pm(R)$:

$$F_\pm(R) = \frac{f_R}{1 + e^{-2s_1(R - s_0)}} \tag{1.13}$$

where s_1 and s_0 are parameters that control the sharpness and location of the switch and $f_R > 0$ is the magnitude of the force. Note that the length of the cell is given by the difference of the endpoints so that the rate of change of length is calculated simply by

$$\dot{L} = \frac{dx_+}{dt} - \frac{dx_-}{dt}. \tag{1.14}$$

where $\cdot$ denotes the time derivative.

Lastly, to determine the velocity field $a(x, t)$ from the forces imposed at the cell ends, we assume that the cell grows isotropically. With isotropic growth, we assume that each elemental tissue volume grows or shrinks by the same factor as the domain changes size. To determine $a(x, t)$, we now change to Lagrangian

coordinates to track the trajectories of elemental tissue volumes. Let $x = \Gamma(X, t)$ be the map that gives the spatial coordinate x for elemental tissue volume X after time t. We specify $\Gamma(X, 0) = X$ so that the initial position of each element X is X. Note that the flow a is related to the map Γ:

$$\frac{\partial \Gamma}{\partial t} = a(X, t). \tag{1.15}$$

We can re-state the isotropic growth assumption in terms of shrinking or growing each elemental tissue element equally over time. That is, the position x, of each elemental tissue volume X is given by

$$x = \Gamma(X, t) = Xr(t), \tag{1.16}$$

where $r(t)$ is the factor that shrinks or grows each material coordinate over time. In this case, since our domain has already been scaled to length 1, $r(t) = L(t)$ is the non-dimensional domain length. The length L is determined by the mechanical model given above. Using Equation (1.15), Equation (1.16), and $r(t) = L(t)$, we find that the flow $a(x, t)$ is related to the domain length $L(t)$ by:

$$a = \frac{\partial \Gamma}{\partial t} = \frac{\partial}{\partial t} XL = X\dot{L} = x\frac{\dot{L}}{L}. \tag{1.17}$$

1.3.1 Transforming the 1D mechanochemical model to a stationary domain

To numerically simulate the 1D mechanochemical model, we transform the moving-boundary problem to a stationary domain. We numerically solve the mechanochemical model on the stationary domain and later transform the solution back to the moving-domain.

Our problem is of the form of a reaction-advection-diffusion PDE system on the domain $\Omega(t) = [x_-(t), x_+(t)]$:

$$R_t + (aR)_x = (DR_x)_x + f(R, R_i), \tag{1.18a}$$
$$R_{it} + (aR_i)_x = (D_i R_{ix})_x - f(R, R_i), \tag{1.18b}$$

where subscripts denote partial derivatives and boundary conditions are

$$R_x|_{x=x_-(t),x_+(t)} = R_{ix}|_{x=x_-(t),x_+(t)} = 0. \tag{1.19}$$

We transform the moving boundary problem to a stationary domain $[0, 1]$. Let $\bar{x} = \frac{x - x_-(t)}{L(t)}$ where $L(t) = x_+(t) - x_-(t)$ is the cell's length. The transformation is given by the map

$$(x, t) \mapsto \left(\bar{x} = \frac{x - x_-(t)}{L(t)}, \bar{t} = t \right) \tag{1.20}$$

so that $\bar{x} \in [0, 1]$. Note that $x = \bar{x}L(t) + x_-(t)$ and $t = \bar{t}$.

We define new variables on the transformed coordinates to match the values in the old coordinates:

$$\bar{R}(\bar{x}, \bar{t}) := R(x(\bar{x}, \bar{t}), t(\bar{x}, \bar{t})), \tag{1.21a}$$
$$\bar{R}_i(\bar{x}, \bar{t}) := R_i(x(\bar{x}, \bar{t}), t(\bar{x}, \bar{t})). \tag{1.21b}$$

Under this transformation (details only shown for R, since everything is similar for R_i), we find that:

$$\bar{R}_{\bar{x}} = R_x x_{\bar{x}} + R_t t_{\bar{x}} = R_x L + R_t 0 = R_x L \tag{1.22a}$$
$$\bar{R}_{\bar{t}} = R_x x_{\bar{t}} + R_t t_{\bar{t}} = R_x(\bar{x}\dot{L} + \dot{x_-}) + R_t 1 = R_x(\bar{x}\dot{L} + \dot{x_-}) + R_t. \tag{1.22b}$$

Using the fact that $a = x\frac{\dot{L}}{L}$, and the above relationships we find that the PDE for $\bar{R}$ is:

$$\bar{R}_{\bar{t}} - \frac{1}{L}\bar{R}_{\bar{x}}(\bar{x}\dot{L} + \dot{x_-}) + \frac{1}{L}\left[\bar{R}(\bar{x}L + x_-)\frac{\dot{L}}{L}\right]_{\bar{x}} = \frac{D}{L^2}\bar{R}_{\bar{x}\bar{x}} + f(\bar{R}, \bar{R}_i). \tag{1.23}$$

We expect the advection term to disappear under this transformation since the domain is now stationary and a term representing concentration or dilution of Rac to appear since the total mass is conserved. Indeed, after simplification, we obtain the reaction-diffusion PDE:

$$\bar{R}_{\bar{t}} = \frac{D}{L(t)^2}\bar{R}_{\bar{x}\bar{x}} + f(\bar{R}, \bar{R}_i) - \bar{R}\frac{\dot{L}(t)}{L(t)}, \tag{1.24}$$

where the diffusion coefficient is depends on the current domain size $L(t)$, and Rac is either concentrated ($-\bar{R}\frac{\dot{L}(t)}{L(t)} > 0$ if the domain is shrinking, $\dot{L}(t) < 0$) or diluted ($-\bar{R}\frac{\dot{L}(t)}{L(t)} < 0$ if the domain is expanding, $\dot{L}(t) > 0$).

Taken together, we find that the PDE model to simulate on $\bar{x} \in [0, 1]$ is

$$\bar{R}_{\bar{t}} = \frac{D}{(L(t))^2}\bar{R}_{\bar{x}\bar{x}} + f(\bar{R}, \bar{R}_i) - \bar{R}\frac{\dot{L}(t)}{L(t)}, \tag{1.25a}$$

$$\bar{R}_{i\bar{t}} = \frac{D_i}{(L(t))^2}\bar{R}_{i\bar{x}\bar{x}} - f(\bar{R}, \bar{R}_i) - R_i\frac{\dot{L}(t)}{L(t)}, \tag{1.25b}$$

with $\bar{R}_{\bar{x}} = \bar{R}_{i\bar{x}} = 0$ for $\bar{x} = 0, 1$. To determine $L = x_+(t) - x_-(t)$ and $\dot{L} = \dot{x_+}(t) - \dot{x_-}(t)$, we simultaneously solve the system of ODEs for the position of the cell endpoints:

$$\gamma\frac{dx_-}{dt} = k(x_+ - x_- - \ell_0) - F_-(\bar{R}(0, t)), \tag{1.26a}$$

$$\gamma\frac{dx_+}{dt} = -k(x_+ - x_- - \ell_0) + F_+(\bar{R}(1, t)). \tag{1.26b}$$

Once the solution is numerically approximated in the stationary domain coordinates $(\bar{x}, \bar{t})$ we undo the coordinate transformation, via $x = \bar{x}L(t) + x_-(t)$, to plot the solution in the original space-time coordinates (x, t) as in Figure 4B and C.

1.3.2 Derivation of no-flux boundary conditions

To determine the appropriate boundary conditions for the 1D mechanochemical model, we define variables to be zero outside the domain $\Omega(t)$ and use the Rankine-Hugoniot jump condition to have no-flux across the cell boundary and treating the domain as a moving discontinuity (as in [8]). We only derive the boundary condition for $R(x, t)$ at x_- since the derivation at x_+ and for R_i is similar. Integrating the PDE for R over the domain $x_1 < x_- < x_2$, we have

$$\frac{\partial}{\partial t}\int_{x_1}^{x_2} R\,dx = \int_{x_1}^{x_2}\frac{\partial}{\partial x}\left(DR_x - aR\right)\,dx + \int_{x_1}^{x_2} f\,dx. \tag{1.27}$$

We can split the integral on the left into two parts and evaluate the first integral on the right to find that

$$\frac{\partial}{\partial t}\left(\int_{x_1}^{x_-} R\,dx - \int_{x_2}^{x_-} R\,dx\right) = \left(DR_x - aR\right)\Big|_{x_1}^{x_2} + \int_{x_1}^{x_2} f\,dx. \tag{1.28}$$

Since $R \equiv 0$ outside of $\Omega(t)$, the integration reduces to

$$\frac{\partial}{\partial t}\left(-\int_{x_2}^{x_-} R\,dx\right) = (DR_x - aR)|_{x=x_2} + \int_{x_1}^{x_2} f\,dx. \tag{1.29}$$

Differentiating with respect to time, we find

$$-\int_{x_2}^{x_-} R_t\,dx - R|_{x=x_-}x'_-(t) = (DR_x - aR)|_{x=x_2} + \int_{x_1}^{x_2} f\,dx. \tag{1.30}$$

Finally, in the limit as $x_1 \to x_-(t)^-$ and $x_2 \to x_-(t)^+$, we find

$$-R|_{x=x_-}x'_-(t) = (DR_x - aR)|_{x=x_-}\,. \tag{1.31}$$

Since $a(x_-(t), t) = x'_-(t)$, we cancel terms from the left and ride side to find that

$$\frac{\partial R}{\partial x} = 0 \quad \text{at} \quad x = x_-(t). \tag{1.32}$$

Similar derivations reveal that

$$\frac{\partial R}{\partial x} = \frac{\partial R_i}{\partial x} = 0 \quad \text{at} \quad x = x_-(t), x_+(t). \tag{1.33}$$

1.4 LPA with length as a parameter

To analyze the effect of cell length and basal activation rate on Rac activity in the cell, we study the wave-pinning model in domains of different sizes using Local Perturbation Analysis. In this formulation of the wave-pinning model, we consider the length L as a parameter instead of a variable, and investigate the regimes of behavior (predicted by LPA) in the PDE system. We used this method to produce the LPA bifurcation diagram in Figure 5A.

To incorporate L as a parameter into the wave-pinning model, we start with the reaction-diffusion system describing Rac activity on a fixed domain of length one, i.e., $x \in [0, 1]$. We next considered the PDEs that would govern Rac dynamics on a domain isotropically stretched to length L, i.e., $x \in [0, L]$. That is, we considered the transformation from the domain $[0, 1] \times [0, \infty)$ to $[0, L] \times [0, \infty)$ given by

$$(x, t) \mapsto (\bar{x} = Lx, \bar{t} = t) \tag{1.34}$$

with new variables $\bar{R}$ and $\bar{R}_i$ defined on this new coordinate system as in §1.3.1. Under this transformation, the PDEs are

$$\frac{\partial \bar{R}}{\partial \bar{t}} = \left(b + c\frac{\bar{R}^n}{1 + \bar{R}^n}\right)\bar{R}_i - \delta\bar{R} + \frac{D}{L^2}\frac{\partial^2 \bar{R}}{\partial \bar{x}^2}, \tag{1.35a}$$

$$\frac{\partial \bar{R}_i}{\partial \bar{t}} = -\left(b + c\frac{\bar{R}^n}{1 + \bar{R}^n}\right)\bar{R}_i + \delta\bar{R} + \frac{D_i}{L^2}\frac{\partial^2 \bar{R}_i}{\partial \bar{x}^2}. \tag{1.35b}$$

In this case, the total amount of Rac, T, in this larger domain is now

$$T := \int_0^L \bar{R} + \bar{R}_i\,d\bar{x} = L\int_0^1 R + R_i\,dx = LR_T. \tag{1.36}$$

Thus, to conserve mass in this larger (or smaller domain), the total amount of Rac must be scaled by the length of the domain, i.e., mass is conserved when the total amount of Rac in the new domain is set to $T = \frac{R_T}{L}$.

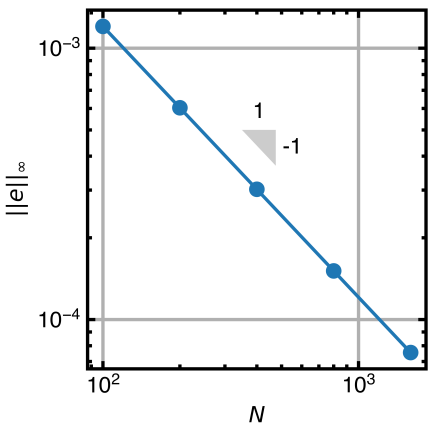

Supporting Figure 2: Validation of mass conservation in the 1D mechanochemical model numerical method. Mass conservation error $\|e\|_\infty$ decreases as the number of spatial grid points N increases. Slope marker (inset) indicates that $\|e\|_\infty = O(N^{-1})$. Parameters and initial conditions are as in Figure 4C, except the final time is $t = 500$.

We now apply LPA to Equation (1.35) to find the following system of ODEs describing the evolution of the global $\bar{R}$ and $\bar{R}^\ell$ local variables with cell length L as a parameter.

$$\frac{d\bar{R}}{d\bar{t}} = \left(b + c\frac{\bar{R}^n}{1+\bar{R}^n}\right)\left(\frac{R_T}{L} - \bar{R}\right) - \delta\bar{R}, \tag{1.37a}$$

$$\frac{d\bar{R}^\ell}{d\bar{t}} = \left(b + c\frac{(\bar{R}^\ell)^n}{1+(\bar{R}^\ell)^n}\right)\left(\frac{R_T}{L} - \bar{R}\right) - \delta\bar{R}^\ell. \tag{1.37b}$$

2 1D numerical methods

We used a method of lines discretization as described in the paper. We validated the numerical methods in 1D by checking for Rac mass conservation over time. We found that the mass conservation error, defined by

$$\|e\|_\infty = \max_t \left| \int_\Omega R + R_i \, dx - R_T \right|, \tag{2.1}$$

is $O(N^{-1})$ (see Figure 2).

3 2D Model

3.1 2D wave-pinning model for Rac GTPase activity

We use the same "wave-pinning" model in §1.1 to describe Rac GTPase activity for active Rac ($\tilde{R}(\tilde{x},\tilde{y},\tau)$) and inactive Rac ($\tilde{R}_i(\tilde{x},\tilde{y},\tau)$) in a 2D domain $\tilde{\Omega} = \{(\tilde{x},\tilde{y}) \in \mathbb{R}^2 \mid \tilde{x}^2 + \tilde{y}^2 \leq \frac{r_0^2}{\pi}\}$ with no-flux boundary conditions on $\partial\tilde{\Omega} = \{(\tilde{x},\tilde{y}) \in \mathbb{R}^2 \mid \tilde{x}^2 + \tilde{y}^2 = \frac{r_0^2}{\pi}\}$. The system of 2D reaction-diffusion PDE governing

the Rac dynamics are:

$$\frac{\partial \tilde{R}}{\partial \tau} = \left(\tilde{b} + \tilde{c}\frac{\tilde{R}^n}{R_0^n + \tilde{R}^n}\right)\tilde{R}_i - \delta\tilde{R} + \tilde{D}_{\tilde{x}}\frac{\partial^2 \tilde{R}}{\partial \tilde{x}^2} + \tilde{D}_{\tilde{y}}\frac{\partial^2 \tilde{R}}{\partial \tilde{y}^2}, \tag{3.1a}$$

$$\frac{\partial \tilde{R}_i}{\partial \tau} = -\left(\tilde{b} + \tilde{c}\frac{\tilde{R}^n}{R_0^n + \tilde{R}^n}\right)\tilde{R}_i + \delta\tilde{R} + \tilde{D}_{i,\tilde{x}}\frac{\partial^2 \tilde{R}_i}{\partial \tilde{x}^2} + \tilde{D}_{i,\tilde{y}}\frac{\partial^2 \tilde{R}_i}{\partial \tilde{y}^2}. \tag{3.1b}$$

Here, the only distinction between the 1D "wave-pinning" model in §4.1 are the diffusion coefficients $\tilde{D}_{\tilde{x}}$, $\tilde{D}_{\tilde{y}}$, $\tilde{D}_{i,\tilde{x}}$, $\tilde{D}_{i,\tilde{y}}$ of the active and inactive forms in the $\tilde{x}$ and $\tilde{y}$ directions, respectively. Due to isotropy, diffusion coefficients in the $\tilde{x}$ and $\tilde{y}$ directions are indistinguishable such that $\tilde{D}_{\tilde{x}} = \tilde{D}_{\tilde{y}} = \tilde{D}$, and $\tilde{D}_{i,\tilde{x}} = \tilde{D}_{i,\tilde{y}} = \tilde{D}_i$

Similarly to 1D, we have assumed that the total amount of Rac is conserved within the cell. Adding Equation (3.1a) to Equation (3.1b), integrating over the domain $\tilde{\Omega}$, and using the boundary conditions gives

$$\int_{\tilde{\Omega}} \tilde{R}(\tilde{x},\tilde{y},\tau) + \tilde{R}_i(\tilde{x},\tilde{y},\tau)\, d\tilde{x}d\tilde{y} = \tilde{A}_0\tilde{R}_T, \tag{3.1c}$$

where $\tilde{R}_T$ is the mean Rac concentration, $\tilde{A}_0$ is the total Area ($\tilde{A}_0\tilde{R}_T$ is the total amount of Rac). To non-dimensionalize the 2D wave-pinning model, we introduce

$$R = \frac{\tilde{R}}{R_0}, \quad R_i = \frac{\tilde{R}_i}{R_0}, \quad t = \tau, \quad x = \frac{\tilde{x}}{r_0}, \quad \text{and} \quad y = \frac{\tilde{y}}{r_0}. \tag{3.2}$$

Similarly to 1D, we do not scale time by the deactivation rate δ as we wish to explore the effect of δ on the system dynamics. With this scaling, the equations become

$$\frac{\partial R}{\partial t} = \left(b + c\frac{R^n}{1+R^n}\right)R_i - \delta R + D\frac{\partial^2 R}{\partial x^2} + D\frac{\partial^2 R}{\partial y^2}, \tag{3.3a}$$

$$\frac{\partial R_i}{\partial t} = -\left(b + c\frac{R^n}{1+R^n}\right)R_i + \delta R + D_i\frac{\partial^2 R_i}{\partial x^2} + D_i\frac{\partial^2 R_i}{\partial y^2}. \tag{3.3b}$$

where the scaled parameters are

$$b = \tilde{b}, \quad c = \tilde{c}, \quad D = \frac{\tilde{D}}{r_0^2}, \quad D_i = \frac{\tilde{D}_i}{r_0^2}, \quad \text{and} \quad R_T = \frac{\tilde{R}_T}{R_0}. \tag{3.4}$$

Note that the domain changes to $\Omega = \{(x,y) \in \mathbb{R}^2 \mid x^2 + y^2 \leq \frac{1}{\pi}\}$ with no-flux boundary conditions on $\partial\Omega = \{(x,y) \in \mathbb{R}^2 \mid x^2 + y^2 = \frac{1}{\pi}\}$. This scaling results in unitary area $A_0 = 1$. Now, the conservation statement is:

$$\int_{\Omega} R(x,y,t) + R_i(x,y,t)\, dxdy = R_T. \tag{3.5}$$

3.2 2D mechanochemical model

To couple Rac activity and cell mechanics in 2D, we track active ($R(x,y,t)$) and inactive ($R_i(x,y,t)$) Rac activity on a time-dependent domain $\Omega(t)$ with boundary $\partial\Omega(t)$. The displacement of the time-dependent domain is captured by the velocity field $\mathbf{a}(x,y,t)$. The same assumption in the 1D mechanochemical model are made such that (1) tension affects Rac activity, (2) Rac activity affects the velocity field, and (3) tension

is a global quantity. Thus, we consider the following 2D reaction-advection-diffusion model of the wave-pinning system:

$$\frac{\partial R}{\partial t} + \nabla \cdot (R\mathbf{a}) = D\nabla^2 R + f(R, R_i), \tag{3.6a}$$

$$\frac{\partial R_i}{\partial t} + \nabla \cdot (R_i\mathbf{a}) = D_i\nabla^2 R_i - f(R, R_i). \tag{3.6b}$$

The same wave-pinning from the 1D model is used to describe the reaction kinetics function $f(R, R_i)$ (see Equation (1.9)), with the main difference being that the tension is defined as the difference between the area and the rest-area of the cell: $T = A - A_0$.

We again adopt the Rankine-Hugoniot jump conditions:

$$(-D\nabla R + \mathbf{a}R) \cdot \mathbf{n} = 0 \quad \text{for} \quad (x, y) \in \partial\Omega(t) \tag{3.7a}$$

$$(-D_i\nabla R_i + \mathbf{a}R_i) \cdot \mathbf{n} = 0 \quad \text{for} \quad (x, y) \in \partial\Omega(t), \tag{3.7b}$$

where $\mathbf{n}$ is the unit normal to the boundary giving total Rac GTPase conservation:

$$\int_{\Omega(t)} R + R_i \, dxdy = R_T. \tag{3.8}$$

3.2.1 Lagrangian-Eulerian framework

In 2D, domain size changes are no longer assumed to be isotropic and we account for spatially-varying growth and density changes within the finite element mesh domain. Similar to 1D, the reaction-advection-diffusion equations are mapped to Lagrangian coordinates to track the trajectories of elemental tissue volumes with the mapping $\mathbf{x} = \Gamma(\bar{\mathbf{x}}, t)$. In a growing continuum domain, we capture spatial and temporal variations of the mapping $\Gamma(\bar{\mathbf{x}}, t)$ through the differential operators:

$$\boldsymbol{F} = \frac{\partial \Gamma}{\partial \bar{\mathbf{x}}} = \frac{\partial \mathbf{x}}{\partial \bar{\mathbf{x}}}, \tag{3.9a}$$

$$\mathbf{a} = \frac{\partial \Gamma}{\partial t} = \frac{\partial \mathbf{x}}{\partial t}. \tag{3.9b}$$

Where $\boldsymbol{F}$ is the deformation gradient tensor which maps the Euclidean/spatial coordinates $\mathbf{x} = (x, y)$ with domain $\Omega(\mathbf{x}, t)$ onto the Lagrangian/material coordinates $\bar{\mathbf{x}} = (\bar{x}, \bar{y})$ with reference domain $\Omega_0(\bar{\mathbf{x}}, t)$, while $\mathbf{a}$ is the instantaneous flow of the material. Similar to 1D, the 2D moving-boundary problem is transformed into a stationary domain for computational simulations, then the solution is transformed back into the moving domain. New variables are defined on the Lagrangian coordinates system and are defined from the Eulerian coordinate system:

$$\bar{R}(\bar{\mathbf{x}}, \bar{t}) := R(\mathbf{x}(\bar{\mathbf{x}}, \bar{t}), t(\bar{\mathbf{x}}, \bar{t})), \tag{3.10a}$$

$$\bar{R}_i(\bar{\mathbf{x}}, \bar{t}) := R_i(\mathbf{x}(\bar{\mathbf{x}}, \bar{t}), t(\bar{\mathbf{x}}, \bar{t})). \tag{3.10b}$$

Under this transformation, gradients are transformed from the spatial gradients ∇ to the material gradients $\nabla_{\bar{\mathbf{x}}}$ through the deformation gradient tensor $\nabla_{\bar{\mathbf{x}}} = \boldsymbol{F}^T\nabla$, while the temporal derivative is transformed from the Eulerian to the Lagrangian coordinate system using the material flow $\mathbf{a}$ and the material derivative, summarized below:

$$\nabla_{\bar{\mathbf{x}}}\bar{R} = \boldsymbol{F}^T\nabla R + R_t t_{\bar{\mathbf{x}}} = \boldsymbol{F}^T\nabla R + R_t 0 = \boldsymbol{F}^T\nabla R, \tag{3.11a}$$

$$\bar{R}_{\bar{t}} = \nabla R\bar{\mathbf{x}}_{\bar{t}} + R_t t_{\bar{t}} = \mathbf{a}\cdot\nabla R + R_t. \tag{3.11b}$$

Note that $\boldsymbol{F} = \nabla_{\bar{\mathbf{x}}}\mathbf{x}$. Combining these transformations together produces the equation

$$\left.\frac{\partial \bar{R}}{\partial t}\right|_{\bar{\mathbf{x}}} + \bar{R}\nabla\cdot\mathbf{a} = DJ^{-1}\nabla_{\bar{\mathbf{x}}}\cdot\left(J\boldsymbol{F}^{-1}\boldsymbol{F}^{-T}\nabla_{\bar{\mathbf{x}}}\bar{R}\right) + f(\bar{R},\bar{R}_i). \tag{3.12}$$

The divergence of velocity $\nabla\cdot\mathbf{a}$ equivalently described by the Jacobian of the deformation gradient tensor $J = \det(\boldsymbol{F})$ through the relation $\nabla\cdot\mathbf{a} = \frac{1}{J}\frac{\partial J}{\partial t}$. This term describes Rac either concentrating ($-\bar{R}\frac{1}{J}\frac{\partial J}{\partial t} > 0$ if the domain is shrinking, $\dot{J}(t) < 0$) or diluting ($-\bar{R}\frac{1}{J}\frac{\partial J}{\partial t} < 0$ if the domain is expanding, $\dot{J}(t) > 0$). This results in

$$\left.\frac{\partial \bar{R}}{\partial t}\right|_{\bar{\mathbf{x}}} = DJ^{-1}\nabla_{\bar{\mathbf{x}}}\cdot\left(J\boldsymbol{F}^{-1}\boldsymbol{F}^{-T}\nabla_{\bar{\mathbf{x}}}\bar{R}\right) + f(\bar{R},\bar{R}_i) - \bar{R}J^{-1}\frac{\partial J}{\partial t}. \tag{3.13}$$

On the stationary domain, the boundary condition is transformed to the stationary domain using continuum mechanics identities, and is given by

$$\left(J\boldsymbol{F}^{-1}D\boldsymbol{F}^{-T}\nabla_{\bar{\mathbf{x}}}\bar{R}\right)\cdot\mathbf{N} = 0 \quad \text{for} \quad (x,y)\in\partial\Omega_0, \tag{3.14}$$

where $\mathbf{N}$ is the unit normal direction of the membrane in the stationary domain. This formulation is useful for numerical simulations since the entire moving domain reaction-diffusion equation determined by the deformation gradient tensor $\boldsymbol{F}$ in addition to the solution of the reaction-diffusion equations on the fixed domain and the entire deformation gradient tensor $\boldsymbol{F}$ can be determined through solving the linear elasticity equation. In the limit where the domain is modeled as a 1D spring system, the Jacobian simplifies to the length of the domain $J(t) = L(t)$ and $\boldsymbol{F}^{-1}(t) = \frac{1}{J(t)} = \frac{1}{L(t)}$, while $\frac{\partial J}{\partial t} = \frac{\partial L(t)}{\partial t} = \dot{L}(t)$, and the 1D reaction-diffusion PDE on the fixed domain (Equation (1.24)) is recovered.

3.2.2 Linear viscoelastic mechanics equation

We used conservation of momentum to describe the viscoelastic deformation of the cell and obtain the mapping from the undeformed coordinates $\bar{\mathbf{x}}$ to the deformed coordinates $\mathbf{x}$. This mapping is described as the displacement $\mathbf{u}(\mathbf{x},\bar{\mathbf{x}}) = \mathbf{x} - \bar{\mathbf{x}}$ for convenience. For a moving cell on the micron scale, inertial forces ($\ddot{\mathbf{u}}$ terms) are neglected as the cell deforms in a laminar environment and operates in the Stokes regime. Furthermore, there is frictional drag force between the cell and its environment captured by the Stokes drag coefficient γ. From this, we write the continuity equation in a pseudo-steady-state:

$$\nabla\cdot\boldsymbol{\sigma} + \gamma\dot{\boldsymbol{u}} = 0, \tag{3.15}$$

where $\boldsymbol{\sigma}$ is the Cauchy stress. Rac activity results in protrusion in the normal direction to the boundary of the moving domain:

$$\boldsymbol{\sigma}^T\mathbf{n} = F_{\pm}(R)\mathbf{n} \quad \text{on} \quad \partial\Omega(t). \tag{3.16}$$

Here, $F_{\pm}(R)\mathbf{n}$ describes polymerization force from actin due to high levels of Rac GTPase activity described in Equation (1.13) along the unit normal $\mathbf{n}$ direction of the membrane, where $\mathbf{n}$ is calculated from the stationary domain normal vector $\mathbf{N}$ using the following transformation: $\mathbf{n} = \mathbf{F}^{-T}\mathbf{N}/\|\mathbf{F}^{-T}\mathbf{N}\|$. We use the Kelvin-Voigt constitutive equation to decompose the Cauchy stress into elastic and viscous elements:

$$\boldsymbol{\sigma} = \boldsymbol{\sigma}^e + \boldsymbol{\sigma}^v. \tag{3.17}$$

For the elastic stress tensor, we start with the generalized Hooke's law constitutive equation for linear elasticity using the elastic compliance tensor $\boldsymbol{C}$ and small-scale strain $\boldsymbol{\varepsilon}$:

$$\boldsymbol{\sigma}^e = \boldsymbol{C}\boldsymbol{\varepsilon}. \tag{3.18}$$

For linear isotropic materials, the elastic compliance tensor $\boldsymbol{C}$ is defined by the Lamé coefficients, λ and μ, for the dilation and shear moduli respectively:

$$\boldsymbol{\sigma}^e = \lambda \text{tr}(\boldsymbol{\varepsilon})\boldsymbol{I} + 2\mu\boldsymbol{\varepsilon}. \tag{3.19}$$

The Lamé coefficients, λ and μ, are material parameters equivalent to the Young's modulus E and Poisson's ratio ν through the relations:

$$\lambda = \frac{E\nu}{(1+\nu)(1-2\nu)}, \tag{3.20a}$$

$$\mu = \frac{E}{2(1+\nu)}. \tag{3.20b}$$

Furthermore, we assume 2D plane stress conditions: $\sigma^e_{31} = \sigma^e_{13} = \sigma^e_{32} = \sigma^e_{23} = \sigma^e_{33} = 0$. For the viscous stress tensor, we start with the generalized linear constitutive equation for viscosity using the viscous compliance tensor $\boldsymbol{G}$ and small-scale strain rate $\dot{\boldsymbol{\varepsilon}}$:

$$\boldsymbol{\sigma}^v = \boldsymbol{G}\dot{\boldsymbol{\varepsilon}}. \tag{3.21}$$

For linear isotropic materials, the viscous compliance tensor $\boldsymbol{G}$ is defined by the equivalent of Lamé coefficients for viscosity, β_λ and β_μ, for the first and second coefficients of viscosity respectively:

$$\boldsymbol{\sigma}^v = \beta_\lambda \text{tr}(\dot{\boldsymbol{\varepsilon}})\boldsymbol{I} + 2\beta_\mu\dot{\boldsymbol{\varepsilon}}, \tag{3.22}$$

The condition of 2D plane stress still applies: $\sigma^v_{31} = \sigma^v_{13} = \sigma^v_{32} = \sigma^v_{23} = \sigma^v_{33} = 0$. We then redefine the first and second coefficient of viscosity in terms of the Lamé coefficients as $\beta_\lambda = \beta_1\lambda$ and $\beta_\mu = \beta_2\mu$. Assuming $\beta_1 = \beta_2 = \beta$, the viscous constitutive equation takes a form parallel to the elastic constitutive equation but for strain rates:

$$\boldsymbol{\sigma}^v = \beta\left(\lambda \text{tr}(\dot{\boldsymbol{\varepsilon}})\boldsymbol{I} + 2\mu\dot{\boldsymbol{\varepsilon}}\right). \tag{3.23}$$

Finally, we relate small-scale strain $\boldsymbol{\varepsilon}$ to the displacement $\boldsymbol{u}$ through

$$\boldsymbol{\varepsilon} = \frac{1}{2}\left(\nabla\boldsymbol{u} + (\nabla\boldsymbol{u})^T\right). \tag{3.24}$$

3.2.3 Coupling reaction-diffusion to mechanics

Once the instantaneous displacement $\boldsymbol{u}$ is determined from the linear viscoelastic mechanics equation, the deformation gradient tensor mapping $\boldsymbol{F} = \frac{\partial \mathbf{x}}{\partial \bar{\mathbf{x}}}$ is obtained from the relation

$$\boldsymbol{F} = \mathbf{I} + \frac{\partial \boldsymbol{u}}{\partial \bar{\mathbf{x}}}, \tag{3.25}$$

where $\mathbf{I}$ is the identity tensor. The deformation gradient tensor $\boldsymbol{F}$, and quantities derivable from the deformation gradient tensor: the Jacobian $J = \det(\boldsymbol{F})$, and the Jacobian rate of change $\frac{\partial J}{\partial t}$ are all the variables required to couple the mechanics to the 2D reaction-diffusion equation on the moving domain. The Rac-dependent force at the boundary is then updated in the mechanics equation through the boundary conditions to couple the reaction-diffusion equations to the mechanics.

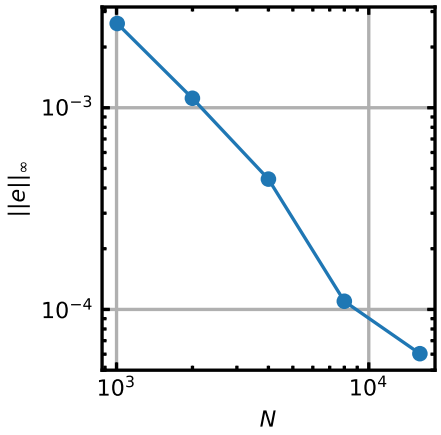

Supporting Figure 3: Validation of mass conservation in 2D mechanochemical model. Mass conservation error $\|e\|_\infty$ decreases as the number of nodes N increases, suggesting that $\|e\|_\infty = O(N^{-1})$. Parameters and initial conditions are as in Figure 6B except the final time is $t = 200$.

3.3 2D numerical methods

We used a finite element method to solve the mechanochemical model as discussed in the paper. Note that a small gradient is introduced to the chemoattractant parameter $b = b_0 + b_1\bar{\mathbf{x}}$ in the material coordinate system to direct the polarization along the x-axis, as polarity can spontaneously occur in any direction depending on the numerical errors of the realization of a simulation.

In coupling the reaction-diffusion to the mechanics, the following happens in a single time step. First, the mechanics equation is solved for that time step. From the displacement, the values of the deformation gradient tensor $\boldsymbol{F}|_t$ and the Jacobian $J|_t$ are obtained. The Jacobian from the previous time step is stored to allow the numerical calculation $\frac{\partial J}{\partial t} \approx \frac{J|_t - J|_{t-1}}{\Delta t}$. These values are then used for the reaction-diffusion time step.

To validate our 2D numerical method, we checked that the total Rac mass is conserved over time. The same definition for error $\|e\|_\infty$ is used from the 1D numerical methods (see Equation (2.1) and Supporting Figure 3).

3.4 2D simulated dynamics

In this section, we show (Supporting Figure 4) how the cell area and cell polarity are related over time for the simulations shown in Figure 6 of the main paper.

4 Chemoattractant gradient simulations

As described in the paper, we simulated 1D and 2D cells migrating up a gradient of chemoattractant encoded in a spatially variable basal activation rate $b(x) = b_0 + b_2 x$. Results show that cells with feedback from tension can migrate further up the gradient before becoming over-saturated and losing polarity (Supporting Figure 5). Here, we eschew the simple $\max R - \min R$ threshold metric used to assess polarity in Figure 5 in the paper and Supporting Figure 4, and instead look at a more detailed investigation into the Rac activity across the cell. At each point in time, a simulated cell in 1D and 2D gives a list of Rac values corresponding to each grid point or node in the spatial discretization. We consider the distribution of these Rac values

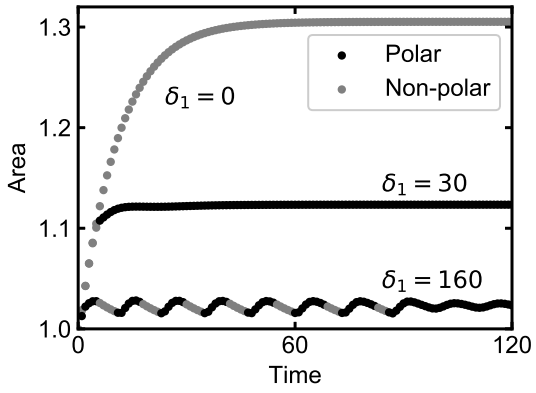

Supporting Figure 4: 2D simulated cell dynamics for different feedback strengths δ_1. Curves show the cell area over time colored by cell polarity (polarized if $\max R - \min R > 0.1$) matching the simulations in Figure 6. Without feedback ($\delta_1 = 0$, $b_0 = 4$) the cell expands to large area without polarizing. With intermediate feedback ($\delta_1 = 30$, $b_0 = 4$) the cell does not expand as much, but does polarize. With strong feedback ($\delta_1 = 160$, $b_0 = 2$) the cell undergoes a polarization-relaxation oscillation until approximately $t = 90$ until the cell remains polarized but oscillates in polarity and area.

and quantify the distribution's interquartile range (IQR; defined as the difference between the 75th and 25th percentile) for each point in time. The motivation for this new metric is that polarized cells (with a region of high Rac activity and a region of low Rac activity) should have bimodal Rac activity distributions. Such distributions will have larger IQR than unimodal Rac activity distributions that would correspond to non-polar cells. Results show that cells with stronger feedback from tension that appear more polarized in Figure 7 in the paper have larger IQR values than cells without feedback in both 1D and 2D (Supporting Figure 5A and B, respectively). In Supporting Figures 6 and 7, we show several snapshots of the Rac activity distribution along with a kernel density estimate (with Gaussian kernel bandwidth = 0.1) corresponding to the 1D and 2D simulations shown in Figure 7 of the paper. These snapshots illustrate how cells without and with feedback become initially polarized (with bimodal distributions) when migrating up the gradient before eventually losing polarity (unimodal distributions). Note that the cells with feedback remain polarized for a longer amount of time.

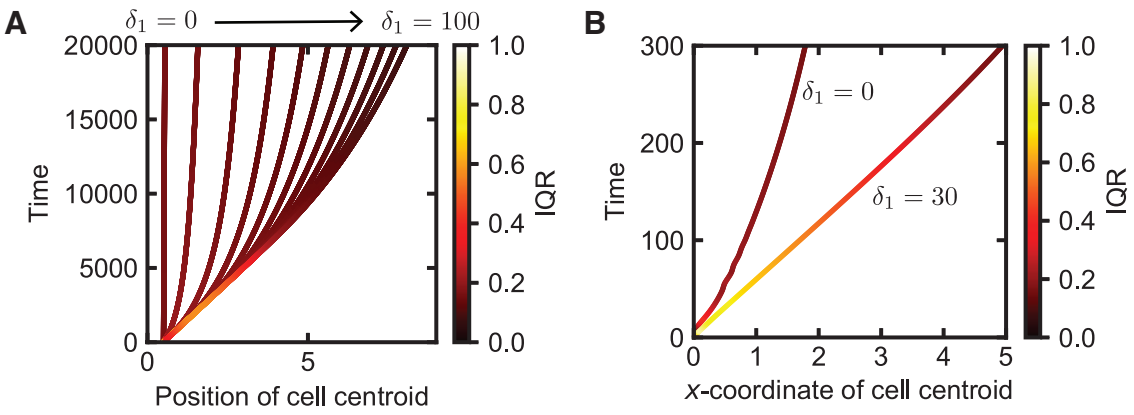

Supporting Figure 5: Position and polarity of simulated 1D and 2D cells in a chemoattractant gradient. **A** The position of cell centroids are shown for 11 one-dimensional cells simulated in the chemoattractant gradient as described in Figure 7 of the paper with $\delta_1 = 0, 10, 20, \ldots, 100$. The color of each curve indicates the polarization of the cell as determined by the interquartile range (IQR) of the Rac activity at that point in time. **B** The x-coordinate of the cell centroids are plotted over time for the two simulated cells in Figure 7B. The 2D cell with feedback from tension is able to migrate further and maintains polarity for longer. Color shows the polarization of the cell (as in A, IQR).

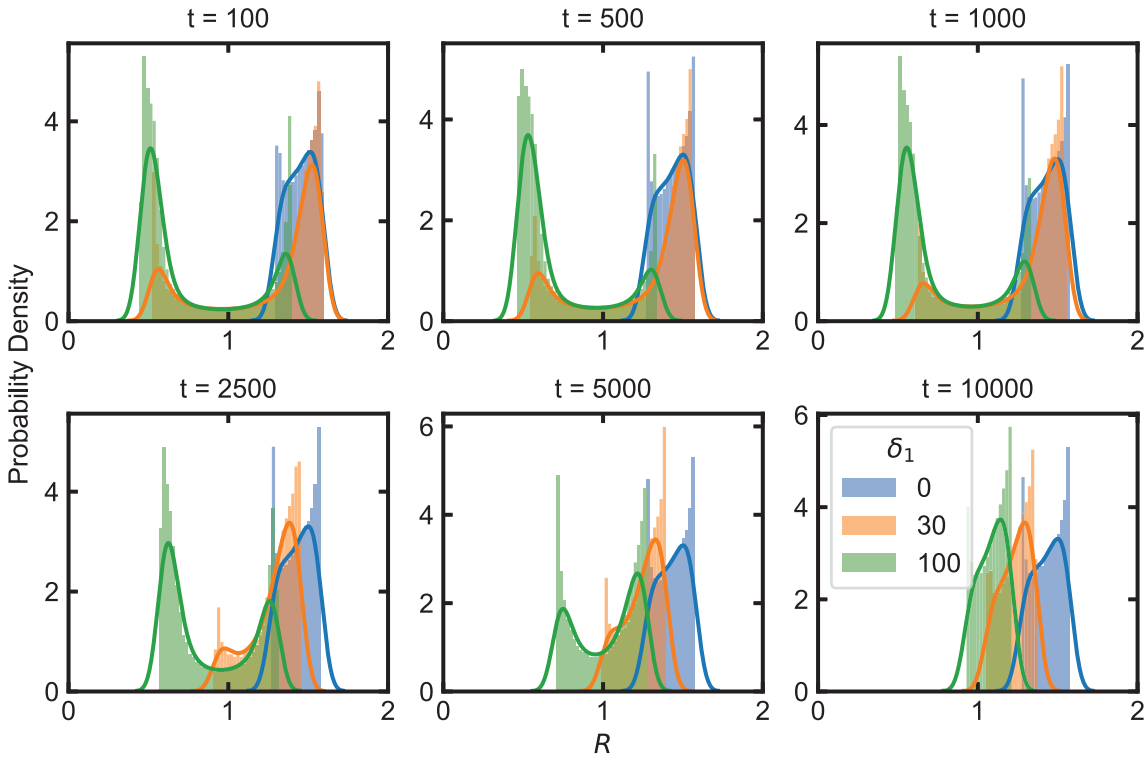

Supporting Figure 6: Snapshots over time of Rac activity distribution and kernel density estimate for 1D simulated cells in a chemoattractant gradient. The Rac activity distributions are shown as normalized histograms for cells simulated in the chemoattractant gradient as described in Figure 7 of the paper with $\delta_1 = 0$ (blue), 30 (orange), and 100 (green) for $t = 100$, 500, 1000, 2500, 5000, and 10000. Kernel density estimates are overlaid. Cells with feedback from tension ($\delta_1 > 0$) have bimodal distributions (therefore have polarized Rac activity) for longer than the cell without feedback ($\delta_1 = 0$). Eventually, all three cells become overstimulated by high Rac activity and lose polarity ($t = 10000$).

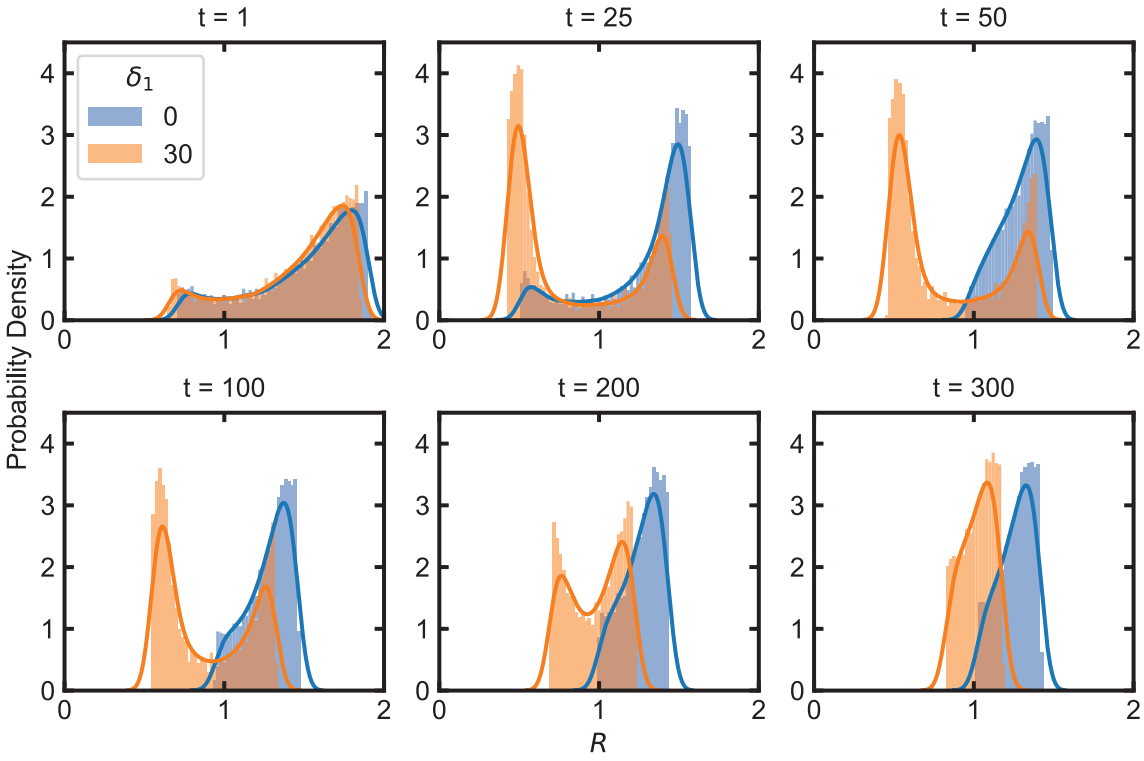

Supporting Figure 7: Snapshots over time of Rac activity distribution and kernel density estimate for 2D simulated cells in a chemoattractant gradient. The Rac activity distributions are shown as normalized histograms for cells simulated in the chemoattractant gradient as described in Figure 7 of the paper with $\delta_1 = 0$ (blue) and 30 (orange) for $t = 1$, 25, 50, 100, 200, and 300. Kernel density estimates are overlaid. Both cells initially polarize (bimodal distributions), and eventually lose polarity (unimodal distributions). The cell with feedback from tension remains polarized for longer. See Movie 9.

Supporting References

[1] Mori Y, Jilkine A, Edelstein-Keshet L. Wave-Pinning and Cell Polarity from a Bistable Reaction-Diffusion System. Biophysical Journal. 2008;94(9):3684–3697. doi:10.1529/biophysj.107.120824.

[2] Holmes WR. An Efficient, Nonlinear Stability Analysis for Detecting Pattern Formation in Reaction Diffusion Systems. Bulletin of Mathematical Biology. 2014;76(1):157–183. doi:10.1007/s11538-013-9914-6.

[3] Holmes WR, Mata MA, Edelstein-Keshet L. Local Perturbation Analysis: A Computational Tool for Biophysical Reaction-Diffusion Models. Biophysical Journal. 2015;108(2):230–236. doi:10.1016/j.bpj.2014.11.3457.

[4] Crampin EJ, Gaffney EA, Maini PK. Reaction and diffusion on growing domains: Scenarios for robust pattern formation. Bulletin of Mathematical Biology. 1999;61(6):1093–1120. doi:10.1006/bulm.1999.0131.

[5] Crampin EJ, Hackborn WW, Maini PK. Pattern Formation in Reaction–Diffusion Models with Nonuniform Domain Growth. Bulletin of Mathematical Biology. 2002;64(4):747–769. doi:10.1006/bulm.2002.0295.

[6] Baker RE, Maini PK. A mechanism for morphogen-controlled domain growth. Journal of Mathematical Biology. 2006;54(5):597–622. doi:10.1007/s00285-006-0060-8.

[7] Buttenschön A, Liu Y, Edelstein-Keshet L. Cell Size, Mechanical Tension, and GTPase Signaling in the Single Cell. Bulletin of Mathematical Biology. 2020;82(2). doi:10.1007/s11538-020-00702-5.

[8] Simon CM, Vaughan EM, Bement WM, Edelstein-Keshet L. Pattern formation of Rho GTPases in single cell wound healing. Molecular Biology of the Cell. 2013;24(3):421–432. doi:10.1091/mbc.e12-08-0634.